

UNIMORE

UNIVERSITÀ DEGLI STUDI DI
MODENA E REGGIO EMILIA

University of Modena and Reggio Emilia

Department of Engineering Enzo Ferrari

Effect of spanwise wall forcing on the separation of a temporal turbulent boundary layer under adverse pressure gradient

Master's Thesis

Candidate:
Maria Elisa Cichero
Student ID: 123456

Supervisor:
Prof. Andrea Cimarelli

Co-supervisor:
Prof. Filippo Moroni

Academic Year 2025–2026

Leave enough room
for wonder.

Abstract

Spanwise wall forcing reduces skin-friction drag in turbulent flows, but its effect on flow separation under adverse pressure gradient (APG) remains to be investigated. The temporal approach has so far been used for APG and for oscillating-wall (OW) boundary layers separately. Here, the two configurations are combined and the analysis is extended to streamwise traveling waves (STW). Direct numerical simulations of a temporally developing turbulent boundary layer are performed. Spanwise forcing is activated at $Re_\tau = 200$, once the initial transient of the temporal boundary layer (Kozul et al. 2016) has ended. Forcing parameters are scaled with a friction velocity averaged over $Re_\tau = 180 - 500$. The APG is imposed as a constant volumetric forcing in the Navier–Stokes equations, with value 7.3610^{-4}, and is activated once the transient of the spanwise forcing has ended, i.e. after four oscillation periods.

OW forcing with $W^+ = 12$ and $T^+ = 100$ yields a drag reduction of 20–25%. Drag increase with OW has been reported only at very long periods ($T^+ > 700$; Quadrio et al. (2009)). In the temporal configuration, such periods allow only about two forcing cycles over the simulated time, which prevents statistical convergence. STW are therefore adopted, since they access the drag-increasing regime at much shorter periods and at a tractable computational cost.

The wave parameters, with $W^+ = 12$, are derived from the forcing map of Quadrio et al. (2009). Periods $T^+ = 100$ and 20 produce drag reduction, up to 15%, whereas $T^+ = 25$ produces a drag increase of about 5%. The maximum drag increase lies near a phase speed $c \approx 0.4$, lower than the value $c \approx 0.5$ reported for channel flow. Separation occurs in all simulated APG cases. The results address whether spanwise forcing promotes separation and show how drag reduction and drag increase affect its onset.

Contents

Abstract **iii**

1 Introduction **1**

2 Temporal turbulent boundary layer **5**

2.1 Kozul's temporal turbulent boundary layer 7

3 Turbulence flow control **11**

3.1 Purely temporal spanwise wall oscillations 12

3.2 Steady-spatial oscillations: space-time conversion 15

3.3 Traveling waves 17

4 Methodology **21**

4.1 Flow settings 21

4.2 Computational domains and grid 23

4.3 Solver and Numerical schemes 24

4.4 Adverse pressure gradient implementation 24

4.5 Inner, outer and external scaling 26

4.6 Forcing parameters 28

4.6.1 Drag performance indexes 28

4.6.2 Oscillating wall parameters 29

4.6.3 Traveling wave parameters 29

4.6.4 Inner-scaled parameters drift in time 32

5 Results **35**

5.1 Simulated cases/overview 35

5.2 TTBL under adverse pressure gradient with spanwise oscillating wall forcing 37

5.2.1 Time evolution and flow quantities 37

5.2.2 Mean velocity profiles 39

5.2.3 Second-order statistics 41
5.3 TTBL under adverse pressure gradient with streamwise traveling wave forcing 50
5.4 Time evolution and flow quantities 50
5.5 Mean velocity profiles 52
5.6 Second-order statistics 53

6 Alternative perspective on drag reduction: momentum flux decomposition 59
6.1 Comparative Momentum Analysis 63

7 Conclusions and future developments 65

Bibliography 67

Chapter 1

Introduction

Reducing aerodynamic drag in wall-bounded turbulent flows is one of the most critical challenges in modern fluid dynamics and in vehicle and aerospace engineering, driven by the urgent need to lower fuel consumption and global CO_2 emissions. Total drag consists primarily of two components: skin-friction drag, which accounts for approximately 50% of the total under attached cruise conditions, and form (pressure) drag, which arises when the flow encounters the body geometry or detaches from the surface. Targeting skin-friction reduction and flow-separation control therefore offers the greatest potential for overall aerodynamic efficiency gains (Ricco et al. 2021).
In canonical wall-bounded flows, turbulent skin friction is generated and maintained by an autonomous near-wall self-sustaining cycle (Schoppa et al. 2002). This cycle involves low-speed velocity streaks and quasi-streamwise vortices located in the buffer layer ($y^+ \leq 30$), which continuously interact to produce violent turbulent bursts and high wall-shear stress (Karniadakis et al. 2003).
When an attached turbulent boundary layer develops over an aerodynamic body, such as an airfoil, a turbine blade or a diffuser, under an adverse pressure gradient (APG), the low-momentum fluid near the surface decelerates rapidly. This can lead to flow separation and to a recirculation bubble characterized by a low-pressure plateau, which degrades lift, increases pressure drag and triggers multi-scale unsteadiness. Managing the near-wall momentum, either to delay detachment or to shorten the separation bubble, is therefore essential to restore pressure recovery and reduce pressure drag.
To mitigate friction drag and control boundary-layer dynamics, a wide variety of flow-control strategies have been developed. They are classified into three primary categories:

1. **Passive control** operates without external energy input. The most prominent passive device is the riblet (a micro-groove sized in wall units, $h^+ \approx 10$–15),

which suppresses spanwise vortex cross-talk and reduces skin-friction drag by 8% to 10% in ideal laboratory settings.

2. **Active closed-loop control** uses real-time feedback from arrays of sensors and actuators to detect and oppose individual turbulent fluctuations. Although theoretically very efficient, dense sensor–actuator networks are currently impractical for real applications.

3. **Active open-loop control** applies a predetermined, deterministic forcing to the fluid without real-time sensing. Key techniques include active suction/blowing and spanwise wall oscillations, introduced in the landmark study by Jung et al. (1992) and extensively investigated by Choi et al. (2001) and Quadrio et al. (2004). By generating an unsteady transverse Stokes layer, this method disrupts the coherence of near-wall streaks and achieves local skin-friction reductions between 30% and 45%.

Although spanwise wall oscillations have been investigated for over three decades, most studies have been performed in turbulent channel flows under zero pressure gradient. Their effect on a boundary layer subject to an adverse pressure gradient, where separation becomes the relevant issue, remains largely unexplored. Addressing this question with high-fidelity simulations poses two main difficulties.

The first is computational. A fully developed channel is statistically homogeneous in the streamwise (x) and spanwise (z) directions, so periodic boundary conditions are sufficient and the cost is moderate. A spatially developing TBL, instead, grows along x: it requires long computational domains, a realistic turbulent inflow and considerable computational resources.

The second is physical. As the boundary-layer thickness $\delta(x)$ grows and the friction velocity u_τ decreases downstream, a forcing with constant physical amplitude and period corresponds to continuously varying viscous parameters (A^+, T^+). The effectiveness of the control then changes along the plate, and inlet transients, Reynolds-number effects and the genuine control effect become mixed together, making the results harder to interpret.

A convenient alternative is the temporally developing boundary layer (TTBL) introduced by Kozul et al. (2016) and recently employed by Moroni et al. (2026) and Cesari (2026). By restoring streamwise periodicity, the TTBL trades spatial growth for temporal growth. Once the effects of the initial condition have decayed ($Re_\theta > 500$), it reproduces the one-point statistics of a spatial TBL at a much lower computational cost. The drift of (A^+, T^+) is not removed, but it now occurs in time and can be tracked explicitly (see Chapter 5).

A further open issue is the lack of a unified explanation of drag reduction in non-canonical flows. Moroni et al. (2026) recently derived an exact momentum flux decomposition showing that the Stokes layer suppresses the outer inviscid velocity jump (ΔU_{nv}), which forces a downward readjustment of the viscous shear stress at the wall. How this mechanism is modified when the boundary layer is also subjected to an adverse pressure gradient has not yet been addressed.

In this context, the primary objective of this thesis is to investigate the interaction between active spanwise wall forcing (specifically wall oscillations and streamwise traveling waves) and the separation of a turbulent boundary layer under an adverse pressure gradient, using a temporal approach and high-fidelity Direct Numerical Simulations (DNS).

It is worth highlighting that streamwise traveling waves allow the investigation of both drag-reduction (DR) and drag-increase (DI) regimes, which is not possible with wall oscillations alone. Unlike purely temporal oscillating walls (OW), where obtaining a drag increase requires extremely long oscillation periods (see Chapter 3) and therefore imposes higher computational costs, streamwise traveling waves give access to the DI regime without extended simulation times.

To address the open questions highlighted above, the present investigation pursues the following goals:

1. **Influence of control on flow separation.** To assess whether, and by how much, wall oscillations and streamwise traveling waves delay or modify separation under an adverse pressure gradient, and how this depends on the forcing parameters.

2. **Validation of the TTBL framework.** To verify that the temporal boundary layer reproduces the expected uncontrolled and controlled statistics, and to quantify how (A^+, T^+) evolve in time during the simulations.

3. **Application of the momentum flux decomposition.** To apply the decomposition of Moroni et al. (2026) to the cases with adverse pressure gradient, in order to identify the mechanisms through which the control alters the wall shear stress.

The outline of this thesis is as follows. Chapter 2 introduces the temporal turbulent boundary layer framework and highlights its advantages over spatially developing configurations. Chapter 3 reviews the state of the art in wall-bounded turbulence control, focusing on spanwise wall oscillations and traveling waves. Chapter 4 details the numerical methods, simulation parameters and validation procedures employed

in this study. Chapter 5 presents the main findings on the effects of spanwise wall forcing on turbulent boundary-layer separation under adverse pressure gradients. Chapter 6 applies the momentum flux decomposition of Moroni et al. (2026) to the study of drag-reduction mechanisms. Finally, Chapter 7 summarizes the key conclusions and outlines directions for future research.

Lastly, the following abbreviations are used throughout this work to identify the different flow-control strategies and simulations: FW denotes the fixed-wall, i.e. uncontrolled, simulation; OW denotes the oscillating-wall simulation; APG denotes the simulation under adverse pressure gradient; OW-APG denotes the simulation under combined wall oscillation and adverse pressure gradient; TW denotes the streamwise traveling wave simulation; TW-APG denotes the simulation under combined streamwise traveling wave and adverse pressure gradient.

Chapter 2

Temporal turbulent boundary layer

In the study of wall-bounded turbulent shear flows, canonical geometries such as channels and pipes have historically served as the primary paradigmatic configurations due to their structural symmetry and statistical homogeneity along the streamwise direction (x).

In numerical simulations, streamwise homogeneity allows for the implementation of periodic boundary conditions. This spatial periodicity simplifies the governing incompressible Navier–Stokes equations, drastically reduces the required physical domain length, and significantly lowers computational costs.

However, turbulent boundary layers (TBLs) possess distinct physical mechanisms that differentiate them from internal channel and pipe flows. Most notably, boundary layers develop in the presence of a free stream, giving rise to a turbulent/non-turbulent interface (TNTI) where the potential outer flow is continuously entrained into the turbulent. This entrainment dynamics and free-boundary interaction render TBLs of paramount relevance for aerodynamic, industrial, and geophysical applications.

Despite their importance, spatially developing turbulent boundary layers (STBLs) present severe computational and theoretical challenges due to their spatial inhomogeneity in the streamwise direction. Moreover, because the boundary layer thickness $\delta(x)$ grows continuously downstream, STBLs cannot naturally accommodate periodic boundary conditions along x. Consequently, numerical simulations of STBLs must explicitly model the streamwise development, introducing two main complications:

1. Inflow boundary conditions and Transition: To simulate a STBL, one must either numerically simulate the laminar-to-turbulent transition process from an inlet trip or employ synthetic inflow generation techniques, such as recycling and rescaling methods (e.g., Lund et al., 1998) or precursor turbulence fields (e.g., Wu and Moin, 2009). These techniques introduce artificial numerical artifacts or require exceptionally long computational domains to allow the flow

to relax into a unmanipulated(steady) turbulent state.

2. Computational costs: Simulating the spatial growth over a sufficient Reynolds number range demands immense streamwise domain lengths. For instance, a spatial DNS reaching a momentum-thickness Reynolds number $Re_\theta \approx 2000$ requires on the order of 3.4×10^9 grid points (Jiménez et al., 2010), placing severe demands on supercomputing resources and slowing down statistical convergence—a limitation that becomes especially acute when studying unsteady or actively controlled flows.

To circumvent the computational and analytical bottlenecks of STBLs, a temporal approach can be adopted. It relies on the implementation of streamwise periodic boundary conditions which allow for the boundary layer to develop in time rather than in space. Streamwise periodicity restores statistical homogeneity in all wall-parallel planes (x-z). As a result, the mean wall-normal velocity vanishes identically everywhere ($v(x, z, t) = 0$), rendering the mean flow parallel to the wall.
While the concept of temporal development has been widely used in free-shear flows (wakes, mixing layers, jets) and internal pipe/channel flows, its application to incompressible boundary layers historically suffered from conceptual limitations (Kozul et al. 2016).
Driven by numerical and physical incentives to employ periodic boundary conditions, Spalart (1988) was among the first to propose an alternative framework for investigating incompressible turbulent boundary layers. He introduced what was later designated as a "spatio-temporal approach", reformulating the Navier–Stokes equations within a coordinate system that expands with the boundary layer growth. When solved with periodic boundary conditions, this system enabled a local approximation of a spatially developing flow. Although pioneering, this formulation introduced extra "growth terms" into the governing equations, resulting in artificial numerical and physical approximations.
Aiming to capitalize on the benefits of periodic boundary conditions, Biau (2023) recently proposed an alternative temporal setup. In this configuration, artificial volumetric body forces are introduced into the governing equations to freeze boundary layer growth, rendering the flow statistically steady. Although this approach provides computationally convenient self-similar profiles, the artificial forcing suppresses the inherent temporal evolution of the boundary layer.

The fundamental formulation of Kozul et al. (2016) resolved these issues by establishing an exact, unapproximated fluid-dynamic framework for the incompressible TTBL.

2.1 Kozul's temporal turbulent boundary layer

To address the limitations of previous temporal methods, Kozul et al. (2016) introduced a pure, unapproximated temporally developing turbulent boundary layer (TTBL) framework. Unlike earlier spatio-temporal approaches that introduced artificial growth terms (Spalart 1988) or volumetric body forces that freeze the boundary layer growth (Biau 2023), Kozul et al. (2016) solve the exact, unmanipulated incompressible Navier–Stokes equations. Physically, Kozul et al. (2016) formulated the TTBL as the exact turbulent counterpart to the classical laminar Rayleigh problem, also known as Stokes' first problem. In this setup, an initially quiescent fluid rests above a flat plate at $y = 0$, which is impulsively set into motion at a constant velocity U_w in the streamwise direction (x). Conversely, in the canonical case, the opposite occurs.

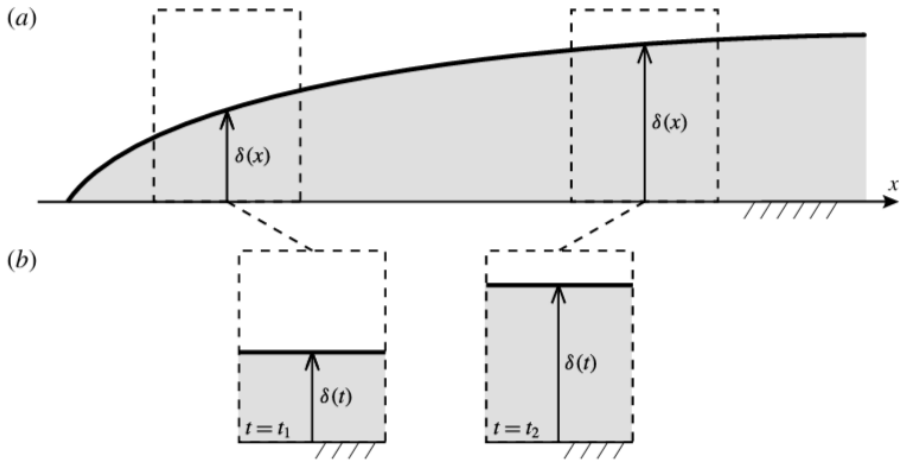


Figure 2.1: Comparison between (a) spatial and (b) temporal turbulent boundary layers Kozul et al. (2016).

By re-mapping the downstream spatial growth $\delta(x)$ into a temporal expansion $\delta(t)$, periodic boundary conditions are enforced along the streamwise (x) and spanwise (z) directions. This wall-parallel periodicity restores statistical homogeneity in (x, z)-planes, causing the mean wall-normal velocity to vanish identically ($\langle V \rangle = 0$) and eliminating mean advection terms from the momentum equations.
To trigger a natural transition to turbulence without numerical artifacts, Kozul et al. (2016) introduced a physically inspired initial velocity profile that models the momentum deficit in the wake of a wall-mounted trip wire of diameter D:

$$U_0(y) = \frac{U_w}{2}\left\{1 + \tanh\left[\frac{D}{2\theta_{sl}}\left(1 - \frac{y}{D}\right)\right]\right\} \tag{2.1}$$

where $\theta_{sl} = 54\nu/U_w$ denotes the momentum thickness of the initial shear layer, and the trip wire diameter scales directly with the initial displacement thickness ($D \approx \delta_0^*$). Low-amplitude white noise ($|u'_{i,0}| < 0.1U_w$) is superimposed near the wall to trigger secondary Kelvin–Helmholtz instabilities.

Through a systematic parametric trip study varying the trip Reynolds number $Re_D = U_w D/\nu$, Kozul et al. (2016) established key foundational results: $Re_D = 500$ is the optimal, lowest trip Reynolds number that successfully forces transition while introducing minimal artificial disturbance, enabling natural boundary layer development at the earliest possible stage. Moreover, as the boundary layer grows such that the ratio of momentum thickness to trip diameter reaches unity ($\theta/D \approx 1$), the flow completely "forgets" its initial tripping footprint. For the $Re_D = 500$ setup, this universal condition is satisfied precisely when $Re_\theta \approx 500$. Beyond this threshold, the TTBL relaxes into an undisturbed, naturally developing fully turbulent state.

Once initial condition effects decay ($Re_\theta > 500$), one-point statistics of TTBL—including skin-friction coefficient ($c_f \sim Re_\theta^{-1/4}$), friction Reynolds number ($Re_\tau \approx 0.93 Re_\theta^{7/8}$), shape factor ($H$), mean velocity profiles (U^+), turbulent variances, Reynolds shear stresses, and higher-order moments up to 4th order (skewness and flatness)—show excellent quantitative agreement with high-fidelity spatial DNS and experimental datasets (e.g., Schlatter and Örlü, 2010; Jiménez et al., 2010). Crucially, TTBL achieves this benchmark accuracy at a fraction of the computational grid requirements (e.g., 0.1×10^9 grid points for TTBL versus 3.4×10^9 for STBL at $Re_\theta \approx 2000$), representing a greater than 30-fold reduction in computational cost

Building upon Kozul's framework, recent investigations have leveraged the TTBL setup to advance the understanding of multi-scale turbulence physics and active flow control strategies.

Moroni et al. (2026) extended the TTBL methodology to evaluate active turbulent drag reduction via harmonic spanwise wall oscillations ($w_w = A\sin(2\pi t/T)$). A critical question addressed in their work was whether a temporal boundary layer accurately reproduces the drag reduction performance and non-equilibrium dynamics of a spatially developing boundary layer under active forcing. They established that while the initial actuation transient is purely temporal in TTBL (governed by tU_w/D) and purely spatial in STBL (governed by $l_x \approx 5\delta_0$), these differences remain strictly confined to the initial transient period. Once the initial transient attenuates, the statistics of TTBL and STBL become identical. Furthermore, Moroni et al. (2026) demonstrated that the simplified transport equations of TTBL enable deeper physical insights into wall control mechanisms. This will be assessed in the following Chapter 5, and will be further exploited to investigate the effects of spanwise wall

forcing on a TTBL under adverse pressure gradient.

To summarize, the unapproximated temporal turbulent boundary layer framework established by Kozul et al. (2016) and validated for complex multi-scale and controlled flows by Cimarelli et al. (2024), Moroni et al. (2026) and Cesari (2026) provides a rigorous, computationally efficient, and mathematically clean surrogate model. It enables the high-fidelity study of canonical boundary layer physics, scale-energy transfers, and wall-bounded flow control while bypassing the computational penalties and inflow complications inherent to spatially developing configurations.

In the present work, this TTBL framework is adopted to investigate the effects of spanwise wall forcing on a turbulent boundary layer under adverse pressure gradient and understand if it represent a valid investigative tool.

Chapter 3

Turbulence flow control

Pioneering studies on wall turbulence highlighted how skin-friction drag reduction originates from coherent structures organized within the viscous sublayer and the buffer layer ($y^+ < 15$). In this region, intermittent events known as sweeps and ejections pair to account for 80% of total kinetic energy and Reynolds stress production. Their definitions are obtained through Quadrant Analysis of the Reynolds shear stress, $-\langle u'v' \rangle$. Sweep events occur in Q4 and consists of high momentum fluid moving toward the wall ($u' > 0, v' < 0$), while ejections occur in Q2 and consist of low momentum fluid moving away from the wall ($u' < 0, v' > 0$).
Later, numerical simulations demonstrated that these events are directly induced by quasi-streamwise vortices situated right above regions of elevated wall-shear stress. Subsequent research established that sweeps and ejections did not represent isolated events: instead, paired together, they dominate the self-sustaining turbulence cycle. Near-wall quasi-streamwise vortices generate and maintain low-speed streaks through lift-up mechanism. As these streaks become unstable, they undergo breakdown and generate new streamwise vortices that feed the cycle again.
Jiménez et al. (1999) proved that this regeneration cycle is strictly confined to the near-wall region and independent from the outer layer dynamics.
Then, Schoppa et al. (2002) refined this physical framework by identifying the precise mechanism governing vortex formation. According to their theory, vortex generation does not originate from streamwise vorticity produced at the wall by either no-slip condition or vorticity roll-up, but rather from the stretching of the near-wall streamwise vorticity sheets. In fact, streaks instability causes vorticity sheets to stretch and collapse into new quasi-streamwise vortices, allowing the cycle to continue.

This chronological sequence of discoveries shaped how researchers approached drag reduction investigations in wall-bounded flows: from weakening already existing

vortices or sweeps, to preventing vortex formation by interrupting the cycle at its origin as suggested by Dhanak et al. (1999), who were among the first to suggest such approach.

Up to this date, transverse forcing strategies, from passive riblets to active wall oscillations and traveling waves, although operating through different actuation mechanisms, all aim to stabilize low-speed streaks, suppress normal vorticity fluctuations and disrupt the phase-locking between streaks and regenerated vortices, thereby halting the near-wall self-sustaining cycle.
Given the purpose of this work, passive control strategies will not be investigated; instead, the state-of-the-art of active open-loop control strategies based on spanwise wall forcing is discussed in detail in the following sections.

3.1 Purely temporal spanwise wall oscillations

The concept of spanwise wall oscillation as an active turbulence control strategy was first introduced by Jung et al. (1992) using Direct Numerical Simulations (DNS) in a turbulent channel flow. By imposing a spatially uniform, time-periodic transverse wall velocity:

$$W_w(t) = A\sin(wt) \tag{3.1}$$

They demonstrated that this unsteady forcing effectively attenuated near-wall turbulence, achieving a skin-friction drag reduction (DR) of up to 40% at a non-dimensional period of $T^+ \approx 100$.
Subsequent numerical and experimental investigations specified the physical mechanisms governing this suppression. Dhanak et al. (1999) and Choi et al. (2001) established that the transverse wall motion laterally shifts near-wall low-speed streaks relative to the overlying quasi-streamwise vortices. This cyclic displacement disrupts the spatial coherence and phase-locking required for streak breakdown, reducing the frequency and duration of high-shear sweep and ejection events by 47% to 78%. Wind-tunnel experiments, such as those by Laadhari et al. (1994) and Choi et al. (1998), provided early physical confirmation of this phenomenon in turbulent boundary layers, visually documenting the characteristic tilting of near-wall streaks.
From a theoretical perspective, fluid motion induced above an oscillating boundary generates an unsteady viscous layer described by Stokes (1851) second problem. For over 140 years, Stokes' solution represented a classical fluid dynamic concept linked to the laminar regime. In the early 2000s, studies by Quadrio et al. (2004), revealed a fundamental theoretical link: in turbulent flows, the phase-averaged mean

transverse velocity profile matches the classical analytical laminar Stokes solution almost perfectly. This agreement arises because, in the viscous layer ($y^+ < 10$), transverse Reynolds shear stress fluctuations ($-\langle v'w' \rangle$) decay as $O(y^3)$ and become negligible relative to viscous diffusion. Consequently, along the spanwise direction the flow behaves like a laminar one, allowing equation 3.1 to give accurate estimation of spanwise shear layer thickness and power required to generate wall motion.
Experiments and numerical simulations over the years helped reach a deeper understanding of the stokes layer effects on the autonomous self-sustaining cycle. This unfolds in three processes: first, the periodic tilting and reorientation of low-speed streaks, where the rapidly changing transverse shear ($T^+ \approx 100$) disrupts structural coherence faster than streaks can reorganize; second, the suppression of wall-normal vorticity fluctuations (ω_y') confined within the viscous sublayer ($y^+ < 15$), which prevents sinuous streak instability and halts vortex regeneration at its onset; and third, the spatial decoupling between streaks and overriding vortices, which breaks phase-locking between sublayer streaks and buffer-layer vortices ($y^+ \approx 15 - 30$), dampening ejection ($Q2$) and sweep ($Q4$) events to sharply reduce Reynolds shear stress $-\langle u'v' \rangle^+$.

Effectiveness of control critically depends on the period and amplitude of wall oscillations. Simulations and experiments have demonstrated the existence of an optimal oscillation period within the range $T^+ \approx 100 - 125$ (Viotti et al. 2008). From a physical point of view, for an oscillation period close to $T^+ \approx 100$, the penetration thickness of the unsteady Stokes layer reaches $y^+ \approx 15 - 20$, which corresponds to the characteristic height of the buffer layer. The timescale of the forcing matches the natural lifetime and self-regeneration timescale of near-wall turbulent structures. Under these optimal conditions, the Stokes layer disrupts streak coherence before the low-speed streaks have sufficient time to reorganize, yielding maximum skin-friction drag reductions between 40% and 45%.
When the oscillation period is excessively short ($T^+ < 50$), the Stokes layer remains extremely thin ($y^+ < 5$) and is confined beneath the primary interaction region between streamwise vortices and streaks, thereby reducing control effectiveness. Conversely, for periods exceeding $T^+ > 400$, the Stokes layer penetrates deeper into the logarithmic region, introducing additional strain that stimulates turbulence production rather than suppressing it. For very long periods ($T^+ \approx 1000$), approaching a steady flow condition, the interaction with turbulence inverts and causes a drag increase estimated between +5% and +10% (Quadrio et al. 2009; Ricco et al. 2021).
Regarding the influence of amplitude, drag reduction increases monotonically with W_w^+, though it exhibits a progressive saturation effect around $W_w^+ \approx 15 - 20$, beyond

which further increases in wall velocity yield negligible additional benefits. In the evaluation of technological feasibility, the net power saved is a crucial parameter. It is defined as the difference between the power saved due to drag reduction and the power spent to actuate the wall motion. Since the required actuation power scales quadratically with the amplitude, a positive net energy saving can only be obtained at low oscillation amplitudes ($W_w^+ < 10$), where it reaches a modest peak between 7% and 10% (Quadrio et al. 2004; Ricco et al. 2021).

While channel flows have served as historical benchmarks for turbulence control due to reasons explained in the previous chapter, real-world engineering applications predominantly involve boundary layers. Moreover, experimentally, establishing a fully developed turbulent channel flow at high Reynolds number is remarkably difficult, whereas turbulent boundary layers over flat surfaces can be implemented with relative ease in wind tunnels (Laadhari et al. 1994).
As a boundary layer grows downstream over a flat plate, the unactuated friction velocity $u_\tau(x)$ continuously decreases. Consequently, maintaining a constant physical wall velocity W_w and period T induces a continuous downstream drift in the inner-scaled parameters $A^+(x)$ and $T^+(x)$. Numerical simulations of TBLs under wall oscillations Yudhistitra et al. (2011), Skote (2011), Skote et al. (2019), and Skote (2022) highlighted three primary consequences of this spatial development:

1. Spatial Inlet Transient: Drag reduction does not establish instantaneously at the onset of actuation; it requires an inlet distance of 3 to 5 boundary-layer thicknesses (δ) to reach fully developed control conditions.

2. Downstream Drag Reduction Decay: In a spatially developing boundary layer, once the initial transient is completed, the local drag reduction margin ($DR\%$) exhibits a continuous downstream decay. As a result, the spatially integrated drag reduction achieved in a boundary layer is inherently lower than that observed in canonical channel flows under equivalent initial conditions.

3. Inner-Scaled Parameter Drift: The physical mechanism driving this downstream decay is the growth of the boundary layer, which causes the unactuated friction velocity $u_\tau(x)$ to decrease and the viscous length scale $\nu/u_\tau(x)$ to expand. Consequently, when applying actuation with constant physical parameters (W_w, T, λ_x), the corresponding inner-scaled non-dimensional quantities $(W_w^+, T^+, \lambda_x^+)$ continuously drift downstream, gradually shifting the control away from its optimal viscous parameter combination.

Despite demonstrating robust drag reduction capabilities, purely temporal wall oscillations present two fundamental engineering constraints:

1. Mechanical Feasibility: Oscillating solid boundaries or physical actuators at high non-dimensional frequencies ($T^+ \approx 100$) incurs high acceleration costs, severe inertial loads, and high structural complexity.

2. Energetic Efficiency: The quadratic scaling of required power ($P_{req} \propto (A^+)^2$) restricts positive net power savings ($P_{net} \approx 7\% - -10\%$) to a narrow operational range at low amplitudes.

The need to overcome these limitations has led to the development of new forcing strategies discussed in the following sections. Two leading approaches are space-time conversion and space-time combination. The former converts frequency w in a spatial wavenumber k_x through the convective velocity of turbulent structures thereby generating spatial or steady wall oscillations (see Viotti et al. (2008) and Skote (2011)), while the latter combines temporal and steady wall oscillations into traveling waves (see Quadrio et al. (2009) and Skote (2022)).
Nevertheless, the intrinsic advantages of the temporal approach — extensively discussed in the previous chapter — have recently opened new avenues of investigation. Notably, Kozul et al. (2016) demonstrated that temporal forcing remains a highly valuable tool, enabling the accurate validation of near-wall control dynamics at a significantly contained computational cost.

3.2 Steady-spatial oscillations: space-time conversion

Driven by the need to eliminate time-dependent mechanical actuation that motivated Viotti et al. (2008) introduced a purely spatial forcing strategy in a turbulent channel flow. Their approach replaced unsteady temporal wall motion with a stationary sinusoidal distribution of spanwise velocity along the streamwise coordinate (x), defined as follows:

$$W_w(x) = A \sin(\kappa_x x) \tag{3.2}$$

where $\kappa_x = 2\pi/\lambda_x$ denotes the streamwise wavenumber and λ_x is the streamwise wavelength of the forcing.
This conceptual transition relied on the space-time conversion principle operating within near-wall turbulence. Although the mean streamwise velocity vanishes at the solid boundary ($U = 0$), turbulent velocity fluctuations in the viscous sublayer

and buffer region ($y^+ < 15$) convect downstream at a remarkably uniform phase velocity $U_c^+ \approx 10$ (Kim et al. 1993)). Consequently, an observer moving downstream alongside the convecting turbulent structures experiences the stationary spatial wave as a time-periodic transverse shear perturbation. Through this convective mechanism, hence convective velocity U_c^+, the optimal temporal oscillation frequency $\omega_{opt}^+ \approx 0.05 - 0.06$ (corresponding to $T_{opt}^+ \approx 100 - 125$) maps directly to an optimal spatial wavenumber $\kappa_{x,opt}^+ \approx 0.005 - 0.006$ (corresponding to $\lambda_{x,opt}^+ \approx 1000 - 1250$) following the relation:

$$\kappa_{x,opt}^+ = \frac{\omega_{opt}^+}{U_c^+} \tag{3.3}$$

Analogous to the temporal Stokes layer, Viotti et al. (2008) derived the analytical solution for the resulting Spatial Stokes Layer (SSL) under steady spatial forcing. Remarkably, just as the classical laminar Stokes solution accurately describes the phase-averaged transverse velocity profile in temporally oscillating turbulent flows, the laminar SSL solution matches the mean turbulent spanwise profile almost perfectly. This agreement occurs because transverse Reynolds shear stresses ($-\langle v'w' \rangle$) decay rapidly near the wall ($O(y^3)$) and remain negligible compared to viscous diffusion, enabling the laminar boundary-layer solution to reliably predict the transversal flow dynamics and the power expended at the wall.

Because steady spatial forcing eliminates time-dependent wall acceleration, the power expended to drive the wall against viscous shear is reduced by approximately a factor of two compared to purely temporal oscillations. Consequently, steady spatial oscillations achieve maximum skin-friction drag reductions exceeding 52% at high amplitudes ($A^+ = 20$) and yield positive net energy savings ($P_{net} = DR - P_{req}$) up to 23% at lower amplitudes ($A^+ = 6$), representing a dramatic improvement over the modest 7%–10% net savings achievable with temporal oscillations. Few years later Skote (2011) performed the first Direct Numerical Simulation extending steady spatial oscillations to a spatially developing turbulent boundary layer over a flat plate ($Re_\theta = 532$) and demonstrating that steady spatial forcing remains highly effective in open, non-homogeneous shear flows, achieving peak local skin-friction drag reductions of up to 46%. Crucially, Skote (2011) discovered that local drag reduction in a boundary layer is not spatially uniform, but oscillates along x with a wavenumber exactly twice that of the wall forcing ($2\kappa_x$), corresponding to half the forcing wavelength ($\lambda_x/2$).

3.3 Traveling waves

The space-time combination approach, developed to overcome the oscillating walls limitations, is achieved through the implementation of traveling waves of spanwise wall velocity. Initially, Du et al. (2000) and Du et al. (2002) introduced a novel class of active control based on spanwise traveling waves propagating along the transverse direction z in a turbulent channel flow. Instead of physically moving the wall, their approach applied electromagnetic Lorentz body force within conductive fluids, acting directly inside the viscous sublayer:

$$F_z(y, z, t) = Ie^{-y/\Delta} \sin(\kappa_z z - \omega t) \tag{3.4}$$

where I represents the interaction parameter (force magnitude), Δ is the penetration depth exponentially decaying away from the wall, $\kappa_z = 2\pi/\lambda_z$ is the spanwise wavenumber, and $\omega = 2\pi/T$ is the forcing frequency. Because the Lorentz force is confined within the viscous sublayer ($\Delta^+ \approx 1.5 - 3$), it generates an unsteady transverse velocity field without requiring moving mechanical components. As highlighted by Karniadakis et al. (2003), the physical mechanism of spanwise traveling waves relies on the complete disruption of canonical high- and low-speed streak pairs near the wall. In their place, a wide, stabilized ribbon of low-speed fluid is formed, which inhibits turbulent burst events and dramatically attenuates Reynolds shear stress. Despite their effectiveness, spanwise-propagating waves pose significant practical implementation challenges due to the requirement of conductive fluids or complex, spanwise-segmented actuation systems. This limitation naturally motivated the exploration of wave propagation along the streamwise direction x, paving the way for both steady spatial waves and streamwise-traveling waves.
While investigating steady spatial waves—see previous section —Quadrio et al. (2009) introduced a comprehensive framework based on streamwise traveling waves (STW) propagating along x:

$$W_w(x, t) = A \cos(\kappa_x x - \omega t) \tag{3.5}$$

This actuation law naturally incorporates purely temporal wall oscillations (OW) as the limiting case where the streamwise wavenumber vanishes ($\kappa_x = 0$), and steady spatial oscillations (SW) as the limiting case where the forcing frequency vanishes ($\omega = 0$). In (3.5), the wave moves backward or forward in the streamwise direction depending on the sign of the phase speed:

$$c = \omega/\kappa_x \tag{3.6}$$

where $c > 0$ corresponds to forward-traveling waves and $c < 0$ corresponds to backward-traveling waves.
By performing an extensive campaign of over 250 Direct Numerical Simulations (DNS) at $Re_\tau = 200$, Quadrio et al. (2009) constructed the foundational two-parameter map of skin-friction drag reduction across the entire $\omega - \kappa_x$ plane, providing the definitive benchmark for active transverse turbulence control.
To explain the physical mechanisms governing the whole parameter space, Quadrio et al. (2009) introduce the concept of the equivalent period defined as:

$$\mathcal{T} = \frac{\lambda_x}{U_c - c} \tag{3.7}$$

The authors describe $\mathcal{T}$ as the time required by the near-wall structures to cover the distance of one wavelength λ_x along the streamwise direction at the relative velocity $U_c - c$. The equivalent period $\mathcal{T}$ dictates whether the forcing disrupts or reinforces the near-wall turbulence regeneration, organizing the flow response in two distinct regimes:

1. Drag reduction: Backward-traveling waves yield consistent drag reduction across all wave speeds because the relative motion between the wave and the convecting streaks is always energetic ($\mathcal{T}$ remains small). For forward-traveling waves, extraordinary performance occurs when waves propagate at slow phase speeds ($c \approx 2 - 3$), where the equivalent period matches the natural optimal timescale of the near-wall cycle ($\mathcal{T}^+ \approx 100 - 125$). Crucially, slow forward waves operate with exceptional energetic efficiency, yielding positive net power savings ($P_{net} = DR - P_{req}$) up to 23%–26% at lower amplitudes ($W_w^+ = 6$). Physically, compared to the canonical, highly coherent streamwise-elongated streaks of unactuated flows, low-speed streaks in the DR regime appear weakened, shortened, and laterally disrupted, preventing streak breakdown and suppressing near-wall Reynolds stress.

2. Drag increase: Conversely, when forward-traveling waves propagate at a phase speed comparable to the convection velocity of near-wall low-speed streaks ($c^+ \approx U_c^+ \approx 10$, Kim et al. (1993)), the denominator in the equivalent period approaches zero ($\mathcal{T}^+ \to \infty$). Physically, instead of being disrupted, the near-wall streaks undergo a pronounced periodic spatial modulation locked to the forcing wavelength λ_x, creating synchronized wavy structures that amplify quasi-streamwise vortices and turbulent momentum transport. This resonance strengthens near-wall streamwise vorticity and produces substantial skin-friction drag increases up to +20% to +23%.

While the channel-flow investigations described so far have established the theoretical and parametric foundations of streamwise-traveling waves, real-world aerodynamic applications involve open, spatially developing turbulent boundary layers (TBL). To bridge the gap between channel flow and boundary layer dynamics, Skote (2015b, 2022) performed Direct Numerical Simulations of a flat-plate turbulent boundary layer demonstrating that the optimal traveling-wave parameters established in channel flows by Quadrio et al. (2009) translate effectively to boundary layer environments. However, streamwise-traveling waves in sTBLs remain subject to the characteristic spatial limitations previously observed for TBLs and pure spanwise oscillations. Specifically, the control experiences an initial spatial transient region—requiring 3 to 5 boundary layer thicknesses (δ) for drag reduction to fully establish—followed by a downstream decay of the drag-reduction margin ($R\%$), driven by boundary layer thickening and the resulting drift in the inner-scaled parameter values. Notwithstanding these spatial constraints, flow visualizations in boundary layers confirm that the fundamental physical mechanism remains active. Specifically, Skote et al. (2019) observed that near-wall low-speed streaks undergo continuous periodic tilting aligned with the transverse shear of the Stokes layer. As emphasized in the review by Ricco et al. (2021), this cyclic reorientation disrupts the spatial alignment required for streak breakdown, confirming that the underlying turbulence suppression mechanism operates effectively in boundary layer environments as well.

Building upon the foundational insights established for both channel flows and spatially developing boundary layers, the present work aims to briefly investigate streamwise-traveling waves of spanwise wall velocity by adopting a temporal simulation framework.

Authors	Geometry	Forcing	Main Results
Jung et al. (1992)	Channel	T-OW	$DR \approx 40\%$
Du et al. (2002)	Channel	z-TW	total streaks suppression
Viotti et al. (2008)	Channel	S-OW	spatio-temporal conversion with $U_c^+ \approx 10$
Quadrio et al. (2009)	Channel	x-TW	complete $k_x - w$ map and lock-in identification
Skote (2011)	BL	S-OW	local DR oscillates with duoble wall frequency
Skote (2022)	BL	x-TW	complete

Table 3.1: Summary table of forcing literary evolution. BL - turbulent boundary layer (spatially developing), T-OW - temporal oscillating wall, S-OW - steady spatial oscillating wall, z-TW - spanwise traveling wave, x-TW - streamwise traveling wave.

Chapter 4

Methodology

This chapter describes the flow configurations which all the simulations presented in this work are based on. The same solver and numerical schemes are used by Cesari (2026) and Moroni et al. (2026) which the present work takes as reference and validation for the adopted TTBL framework, OW and APG implemetation.

4.1 Flow settings

The simulation set-up adopted in this work is not new to the literature. Kozul et al. (2016), Zhang et al. (2018), and Zhang et al. (2023) have already employed this configuration, showing good agreement between its main features and those of spatially developing boundary layers, thereby justifying its use.
The fluid is initially stationary over a solid wall located at the bottom ($y = 0$) which moves with constant velocity U_w in the streamwise direction (x). The flow evolves in time thus presenting spatial homogeneity in the streamwise and spanwise (Z) directions.
The simulations have been carried out using Incompact3d, a Fortran-based CFD solver used mainly for DNS of turbulent flows, developed by Laizet et al. (2009) with the Turbulence, Mixing and Flow Control Group at Imperial College London. It is designed to solve non-dimensional Navier-Stokes equations and therefore receives Re as the only input parameter. The Reynolds number is then used to compute the kinematic viscosity as $\nu = 1/Re$, assuming unitary length and velocity reference scales which vary with the specific flow case. For TTBLs, the Reynolds number is based on the trip wire diameter, D, and the wall velocity, U_w, as follows:

$$Re_D = \frac{U_w D}{\nu}. \tag{4.1}$$

Taking inspiation from wind tunnels, the purpose of the trip wire diameter is to trigger the transition to turbulence. Following Kozul et al. (2016), a value of $Re_D = 500$ is selected to allow for the quickest transient of the initial condition vanishing at $Re_\theta = U_w\theta/\nu = Re_D$, where θ is the momentum thickness of the boundary layer.

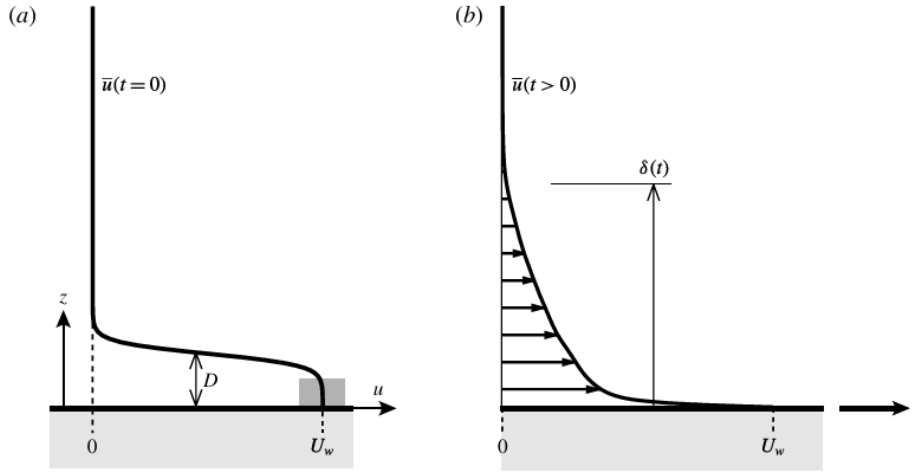


Figure 4.1: Streamwise velocity profile at (a) $t = 0$ and (b) $t > 0$. Grey area on the profile represents the white noise added to trigger transition to turbulence. Figure from Kozul et al. (2016).

To allow dimensional simulations, other parameters, like inlet velocity and domain dimensions, are also provided. Periodic boundary conditions imposed in the x and z directions express the streamwise and spanwise homogeneity previously mentioned. A Dirichlet boundary condition for velocity is applied at the wall in the wall-normal (y) direction imposing $u^*(x, y, z = 0) = 1$ and $v^*(x, y, z = 0) = w^*(x, y, z = 0) = 0$, while a free-slip condition is used at the top of the domain (L_y) through $w^*(x, y, z = L_y) = 0$ and $(\partial u^*/\partial y)|_{L_y} = (\partial v^*/\partial y)|_{L_y} = 0$
Bottom wall BCs vary depending on the presence of flow control as shown in table 2.

	Bottom BCs
uncontrolled cases	$(U_w, 0, 0)$
wall oscillations cases	$(U_w, 0, w_w)$
streamwise traveling waves cases	$(U_w, 0, w_w)$

Table 4.1: Bottom wall boundary conditions vary depending on the flow control type. For both wall oscillations and streamwise traveling waves cases w_w varies with the specific control law following equations 4.2 and 4.3.

When spanwise wall oscillation and streamwise traveling waves are enabled, the

spanwise velocity imposed as bottom wall boundary condition follows the subsequent laws, respectively:

$$w_w(t) = A \sin\left(2\pi\left(\frac{t - t_{start,wo}}{t_{wo}}\right) + \phi\pi\right), \tag{4.2}$$

$$w_w(x,t) = A \sin\left(2\pi\left(\frac{x}{\lambda_x} - \frac{t - t_{start,tw}}{t_{tw}}\right) + \phi\pi\right) \tag{4.3}$$

where ϕ is the face shift, superimposed to be null.
The initial condition is represented by a homogeneous hyperbolic tangent streamwise velocity profile,

$$U_{IC}(y) = \frac{U_w}{2} + \frac{U_w}{2} \tanh\left(\frac{D}{2\theta_{sl}}(1 - \frac{y}{D})\right), \tag{4.4}$$

where $\theta_{sl} = 54\nu/U_w$ is the momentum thickness of the initial shear layer. Numerically the transition is achieved by adding white noise to all velocity components. A white noise, with a value of $0.1U_w$ is superimposed to the initial conditions to achieve a faster transition to turbulence.

4.2 Computational domains and grid

Domain dimensions and mesh discretization are reported in table 1.

L_x/D	L_y/D	L_z/D	n_x	n_y	n_z	$\Delta t U_w/D$
265.2	88.4	132.6	384	649	384	0.025

Table 4.2: Domain dimensions and mesh discretization. The same values have been used for all simulated flow cases.

In a temporal approach, the friction Reynolds number $Re_\tau = u_\tau \delta_{99}/\nu$ increases with time, as the boundary layer thickness ($\delta = \delta_{99}$) grows faster than the friction velocity decreases. To prevent the boundary layer from interacting with the upper boundary of the computational domain, appropriate domain dimensions must therefore be imposed. To achieve this, the domain height (wall-normal direction) is set to be four times the final boundary layer thickness δ_f. Consequently, domain dimensions are set to $(L_x, L_y, L_z)\delta_f = (12; 3; 6)$, with δ_f estimated by using data from Cimarelli et al. (2024) at the target (final) Re_τ.
The grid is homogeneous in x and z directions and is stretched in the wall-normal direction with a refinement parameter $\beta = 2.2$ in order to allow for a finer resolution near the wall and a coarser resolution in the outer region. The domain is discretized

with a number of grid points $(N_x, N_y, N_z) = (384, 649, 384)$ thus coarsening the resolution $(\Delta x^+, \Delta y_w^+, \Delta y_d^+, \Delta z^+) = (20.77, 0.317, 0.78, 10.38)$. This set up, validated by Cesari (2026), ensures a stable and accurate results. Time step is set to a value of 0.025 which is sufficient to reach a friction Reynolds number $Re_\tau = 5004$ after 60000 iterations.
The different flow cases simulated and their specifics are reported in table 5.1.

4.3 Solver and Numerical schemes

Spatial integration is performed with 6th order compact finite difference schemes for both convective and diffusive terms. For the viscous term, the hyperviscous version of the standard 6th order compact finite difference scheme is used.
Time integration is performed using third-order Runge-Kutta scheme ($RK3$) for convective terms; for diffusive terms in y direction implicit time integration is available with the second-order Crank-Nicholson scheme (CN). This mixed approach allows to the drop stability parameter S, $S = u_{ref}^2 \Delta t / 2\nu$, restriction which applies strictly for fully explicit schemes. For TTBLs, $u_{ref} = U_w$. With implicit diffusion for y direction terms, the hyperviscous operator for the second order derivative can be used only with Dirichlet conditions on both bottom and top boundaries.

4.4 Adverse pressure gradient implementation

To extend the zero-pressure-gradient (ZPG) temporally developing turbulent boundary layer (TTBL) framework — originally formulated by Kozul et al. (2016) — to adverse pressure gradient conditions, this study follows the numerical methodology established by Cesari (2026). In standard ZPG TTBL setups, momentum is exchanged between the moving bottom wall (translating at constant speed $U_{\text{wall}} = 1.0$) and the fluid, strictly via viscous diffusion.
As demonstrated by Cesari (2026) in Section 1.2.2.1 of his thesis, simply decelerating the wall velocity ($dU_{\text{wall}}/dt < 0$) is physically inadequate to model an APG boundary layer. Wall deceleration transmits momentum changes solely through viscous diffusion from the wall surface inward ($\partial^2 u / \partial y^2|_w = \frac{1}{\nu} dU_{\text{wall}}/dt$), whereas an actual adverse pressure gradient decelerates the entire fluid column across the boundary layer thickness. To faithfully reproduce the global flow deceleration characteristic of an APG while maintaining a constant wall speed ($dU_{\text{wall}}/dt = 0$), Cesari (2026) introduced the pressure gradient as an external volumetric momentum forcing (body

force) directly within the incompressible Navier-Stokes equations:

$$\frac{\partial u}{\partial t} + u\frac{\partial u}{\partial x} + v\frac{\partial u}{\partial y} = -\frac{1}{\rho}\frac{\mathrm{d}P_e}{\mathrm{d}x} + \nu\left(\frac{\partial^2 u}{\partial x^2} + \frac{\partial^2 u}{\partial y^2}\right) \tag{4.5}$$

At the wall boundary, this volumetric forcing modifies the local curvature of the mean velocity profile according to:

$$\left.\frac{\partial^2 u}{\partial y^2}\right|_w = \frac{1}{\rho\nu}\frac{\mathrm{d}P_e}{\mathrm{d}x} > 0 \tag{4.6}$$

Numerically, this mechanism is implemented in Incompact3d via dedicated Fortran subroutine. When the pressure gradient is enabled, a uniform volumetric momentum forcing term $\mathrm{d}P_e/\mathrm{d}x = \mathrm{pg_constant} > 0$ is added at each time step directly to the streamwise velocity RHS array.
To evaluate the constant volumetric forcing for a desired APG, the non-dimensional Clauser pressure gradient parameter β is employed, defined as follows:

$$\beta = \frac{\delta^*}{\tau_w}\frac{\mathrm{d}P_e}{\mathrm{d}x} = \frac{\delta^*}{\rho u_\tau^2}\frac{\mathrm{d}P_e}{\mathrm{d}x} \tag{4.7}$$

where δ^* is the displacement thickness, $\tau_w = \rho u_\tau^2$ is the mean wall shear stress, and u_τ is the friction velocity. Inverting this expression the volumetric momentum forcing imposed is obtained:

$$\frac{\mathrm{d}P_e}{\mathrm{d}x} = \beta_{\mathrm{nom}}\,\rho\frac{u_\tau^2}{\delta^*} \tag{4.8}$$

Cesari (2026) evaluated four nominal values of the Clauser parameter $\beta_{\mathrm{nom}} = 0.2, 0.5, 0.7, 1.0$ to better investigate the boundary layer response across mild, moderate and strong deceleration regimes. Among these, the case with $\beta_{\mathrm{nom}} = 1.0$ yielded a constant pressure gradient of 0.000736 successfully promoting separation.
In the present work, to maximize pressure gradient effects, promote flow separation and enable a direct comparison across simulations, the same forcing magnitude is selected across all APG-subjected simulations (APG, OW-APG, and TW-APG). In Cesari (2026), a fundamental distinction between canonical spatial DNS and temporal TTBL simulations is highlighted:

1. Spatial DNS (Kitsios et al. 2016; Kitsios et al. 2017): the APG is imposed via far-field boundary conditions designed to maintain a constant Clauser parameter downstream, generating a self-similar boundary layer free from pressure-gradient history effects.

2. Temporal DNS (Cesari 2026): a constant volumetric pressure gradient is

imposed in time. As the boundary layer expands over time and the wall shear stress decays ($\tau_w \to 0$), the effective Clauser parameter increases continuously.

As demonstrated by Cesari (2026) through diagnostic $H - \beta$ and $H - Re_\theta$ diagrams, the flow is non-self-similar and exhibits pronounced history effects. To allow for a more comprehensive analysis, the boundary layer shape factor H is here presented and defined as the ratio of displacement thickness δ^* to momentum thickness θ:

$$H = \frac{\delta^*}{\theta} \tag{4.9}$$

Physically, the shape factor H serves as a measure of the boundary layer's fullness and its proximity to separation, describing the degree of velocity deficit and profile inflection caused by flow deceleration:

1. For canonical laminar blasius boundary layer, $H \approx 2.59$; in ZPG cases, laminar to turbulent transition is observed with a steep decrease of the shape factor to $H \approx 1.3$.

2. For canonical turbulent ZPG boundary layer, $H \approx 1.3$

3. For turbulent APG boundary layers, H increases with the pressure gradient, reaching values of $H \approx 2.0$ for incipient separation and $H = 2.3 \div 2.8$ for fully separated flows.

Building upon the temporal DNS framework developed by Cesari (2026)—which successfully demonstrated that the temporal formulation accurately reproduces fundamental APG mechanisms—the present work adopts this methodology as a physically robust and computationally efficient foundation for the subsequent numerical investigations.

4.5 Inner, outer and external scaling

A major physical consequence of the APG is the degradation of traditional inner (viscous) scaling. Under ZPG conditions, viscous scales (ν/u_τ and u_τ) effectively collapse the mean velocity and turbulence statistics near the wall, sustaining the universal logarithmic law of the wall. In contrast, under APG conditions, the severe reduction of u_τ causes inner scaling to lose its physical relevance, failing to collapse mean velocity deficit profiles and Reynolds stress distributions. As $u_\tau \to 0$, inner scaling becomes poorly conditioned, necessitating an alternative scaling framework centered on the outer layer dynamics. Under strong APG, the outer region expands

and dominates the overall flow physics, developing a highly pronounced wake region and introducing an inflection point in the mean velocity profile. This mean flow inflection gives rise to a shear-layer-like instability, which promotes the localized generation of turbulent kinetic energy further away from the wall. Consequently, a prominent second outer peak emerges in the velocity variances, Reynolds shear stress $-\langle u'v' \rangle$, and turbulent production profiles. As the pressure gradient intensifies, the flow gradually transitions from a wall-bounded boundary layer toward a free shear layer behavior dominated by large-scale outer structures. To properly capture these outer-dominated dynamics, outer scaling is introduced using characteristic outer velocity scales (such as the freestream velocity U_e in spatial formulations or the wall speed U_w in temporal frameworks) and integral length scales (δ_1, δ_2, or δ_{99}). Direct Numerical Simulations (DNS) of self-similar APG TBLs, such as those performed by Kitsios et al. (2016) and Kitsios et al. (2017), demonstrated that outer scaling successfully collapses mean velocity deficits, Reynolds stress profiles, and energy budgets across various streamwise locations. Building upon these spatial canonical studies, recent investigations on temporally developing TBLs under adverse pressure gradient (e.g., Cesari (2026)) have shown that outer scaling remains robust and physically consistent when extended to temporal formulations.

Therefore, the outer scaling framework is applied in this work to all APG configurations, including those subjected to active wall forcing. Furthermore, by systematically comparing inner and outer scaling representations, this work aims to validate its applicability and assess its physical relevance in capturing the dynamics of APG TBLs under active control.

When evaluating boundary layer statistics under active wall control, standard inner scaling uses the local friction velocity u_τ to normalize flow variables. However, because u_τ decreases during drag reduction, this normalization creates a self-referential effect that masks the true magnitude of flow changes. To overcome this limitation, Moroni et al. (2026) adopt an external scaling, normalizing velocities by a constant reference velocity U_w (or U_∞) and distances by a global length scale D. By removing the modulation of u_τ, external scaling clearly reveals the absolute reduction and outward displacement of turbulent statistics. In the present work, the external scaling framework is applied to all purely spanwise wall forcing cases. Moreover, a systematic comparison between traditional inner scaling and external scaling is carried out to illustrate how inner-scaled statistics capture the local, autonomous behavior of near-wall turbulence, while external scaling uncovers the absolute momentum flux variations and the physical mechanisms driving skin-friction reduction.

4.6 Forcing parameters

The purpose of this section is to provide a comprehensive overview of the forcing parameters employed in the present study, which are crucial for understanding the flow control strategies implemented.
Both oscillations and traveling waves parameters are calculated in inner units, based on the friction velocity u_τ and the viscous length scale ν/u_τ. Friction velocity is calculated as follows:

$$\tau_{xw} = \nu \left| \frac{dU}{dy} \right|_w \qquad u_{\tau,x} = \sqrt{\tau_{xw}} \tag{4.10}$$

where τ_{xw} is the wall shear stress in the streamwise direction and U is the mean streamwise velocity.

4.6.1 Drag performance indexes

When dealing with flow control, its effectiveness is quantified through the drag reduction performance indexes presented hereafter. First, the skin friction coefficient is presented:

$$c_f = \frac{\tau_w}{\frac{1}{2}\rho U_w^2} \tag{4.11}$$

where τ_w is defined in 4.10 and U_w is the wall velocity.
The percentage skin-friction drag reduction is defined as Ricco et al. (2021):

$$DR(\%) = \frac{c_{f,0} - c_f}{c_{f,0}} 100 \tag{4.12}$$

where c_f is the skin friction coefficient of the controlled cases while $c_{f,0}$ is the skin friction coefficient of the reference case (FW). A positive value of DR indicates a reduction in wall shear stress with respect to the reference case, while a negative value indicates an increase in drag, (drag increase, DI). This distinction is important for evaluating the effectiveness of different flow control strategies through this work. In particular, the traveling wave cases have been specifically set to explore both regimes. allowing a direct comparison between DR and DI behaviours.
Given the importance of the temporal approach in this study, DR is calculated through skin-friction coefficient at the same time position tU_W/D, rather than at equal streamwise positions, as is the case for spatial TBLs.

4.6.2 Oscillating wall parameters

Given that the friction velocity varies with time, the scaling of oscillating parameters is performed using the average of the fixed wall case friction velocity in the Re_τ range, $Re_\tau = 180 - 500$, denoted as $\langle u_{\tau,fw} \rangle$.
Consequently, the oscillation amplitude and period are defined as follows:

$$A^+ = \frac{A}{\langle u_{\tau,fw} \rangle} \qquad T^+ = \frac{T \langle u_{\tau,fw} \rangle^2}{\nu} \tag{4.13}$$

In order to ensure a direct comparison with literature results, the present study adopts the optimal oscillation parameters identified by Ricco et al. (2021) for a turbulent boundary layer, which are $A^+ = 12$ and $T^+ = 100$, as reported more extensively in table 5.1. Moreover, this set of values is consistent across both OW and OW-APG cases, allowing for a direct comparison of the effects of adverse pressure gradient on the oscillating wall control strategy.

4.6.3 Traveling wave parameters

Values of traveling wave parameters are selected with reference to the optimal values obtained by Quadrio et al. (2009) for a channel flow. Although previous studies on turbulent boundary layers have been conducted with this type of forcing, (Skote 2022), the work of Quadrio et al. (2009) represents a more comprehensive reference for the present study due to its broader range of available data and results. For the same reason, appropriate re-scaling is applied to ensure that the parameters are consistent with the present boundary layer setup setup. Amplitude and period of traveling waves are defined accordingly to equation 4.13.
First of all, to implement streamwise-traveling waves of spanwise wall velocity (STW), the forcing wavelength λ_x must fit an integer number of times within the computational domain length L_x, in order to satisfy the periodic boundary conditions of the temporal approach. This requirement is enforced by defining the wavelength as:

$$\lambda_x = \frac{L_x}{n_{\text{waves}}} \tag{4.14}$$

where n_{waves} is an integer representing the number of complete waves inside the domain. Within this framework, n_{waves} is specifically selected so that the resulting wavelength λ_x expressed in boundary layer units matches the characteristic wavelengths identified in canonical channel flow studies (e.g., Quadrio et al. (2009)). In particular, this matching targets the optimal parameters responsible for maximum

Drag Reduction (DR) and Drag Increase (DI), corresponding to streamwise wavenumbers $\kappa_x = 4$ and $\kappa_x = 5$, expressed in channel units. Therefore, after appropriate scaling, the following pool of values, $n_{\text{waves}} = 17$ and $n_{\text{waves}} = 21$, matching $\kappa_x = 4$ and $\kappa_x = 5$ respectively, is obtained for the current domain set-up.
Simultaneously, to ensure physical and numerical consistency with the baseline domain configuration established in previous simulations, the total streamwise length L_x is constrained to remain an integer multiple of the final boundary layer thickness, as seen in Chapter 4.
Knowing n_{waves}, hence κ_x, the domain length in the streamwise direction L_x, and the forcing period T_{tw}, the phase speed of traveling waves is calculated as:

$$c = \frac{\omega}{k_x} = \frac{\lambda_x}{T_{tw}} = \frac{L_x}{n_{\text{waves}} T_{tw}} \tag{4.15}$$

In inner units, the wavelength and phase speed are defined as follows:

$$\lambda_x^+ = \frac{\lambda_x \langle u_{\tau,fw} \rangle}{\nu} \qquad c^+ = \frac{\lambda_x^+}{T_{tw}^+} = \frac{c}{\langle u_{\tau,fw} \rangle} \tag{4.16}$$

Literature of streamwise traveling waves defined a range of optimal phase speeds for both DR and DI cases, which are $c^+ 2 \div 3$ and $c^+ 10 \div 13$ respectively. To target those values and specifically identify DI regime, multiple simulations were performed in the present work, varying the two degrees of freedom, n_{waves} and T_{tw}^+, governing equation 4.15. All TW cases are reported in figure 4.3. To better investigate the phase-locking behaviour and the different physical mechanisms between DI and DR only two, among the simulated TW cases, have been selected for a more in-depth analysis namely the DR-01 and DI-02 cases to which this work refers as TW-DR and TW-DI respectively.

Simulation	k	w	DR/DI [%]	t_tw	lam_x	t_avg_start	t_avg_end
DR-01	0.4975	0.3491	+14.91	18.00	12.6286	362.0	1500.0
DR-02	0.4028	0.2793	+13.44	22.50	15.6000	380.0	1500.0
DR-03	0.4028	0.0698	+9.55	90.00	15.6000	650.0	1500.0
DI-01	0.4975	0.2094	-3.61	30.00	12.6286	410.0	1500.0
DI-02	0.4975	0.2793	-4.91	22.50	12.6286	380.0	1500.0
DI-03	0.4028	0.2094	-5.75	30.00	15.6000	410.0	1500.0

Figure 4.2: Summary table of all simulated cases in the pursiut of DI zone identification.

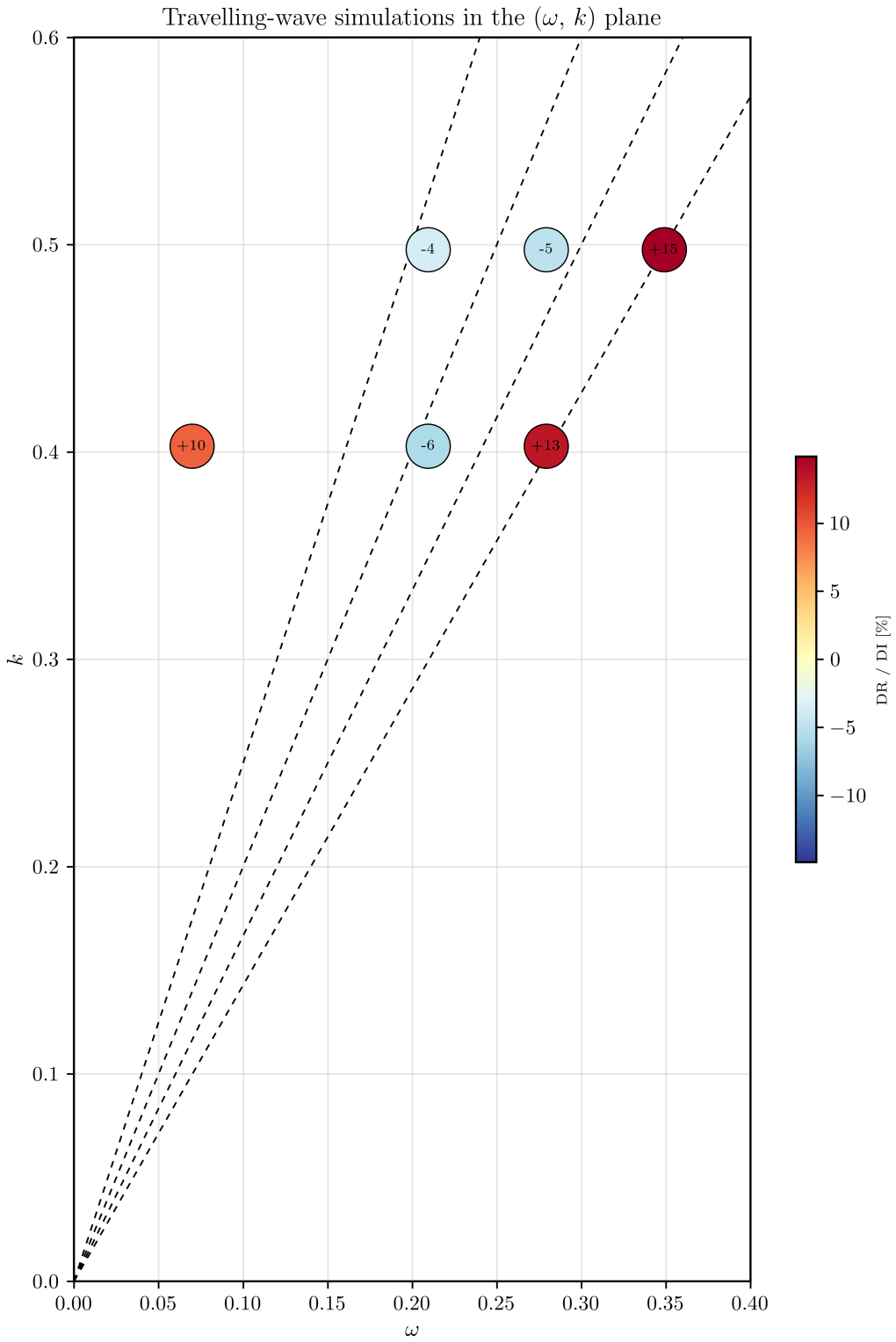


Figure 4.3: Friction drag reduction map in the $w - k_x$ plane for A = 0.5678 of TW simulations. Red values indicate drag reduction; blue values indicate drag increase similarly to figure 2. Quadrio et al. (2009). The numbers indicate the percentage drag reduction rounded to the nearest integer. Dashed lines represent different values of phase speed to better locate the DI zone.

4.6.4 Inner-scaled parameters drift in time

In turbulent boundary layers, unlike in canonical channel flows, variables scaled in inner (viscous) units vary continuously along the flow due to the spatial growth of the boundary layer thickness $\delta(x)$ and the consequent downstream decay of the friction velocity $u_\tau(x)$. When spanwise wall forcing (oscillations or traveling waves) is applied with fixed physical parameters (W_w, T, λ_x), the local inner-scaled parameters mentioned above shift continuously downstream. This drift moves the forcing away from its optimal near-wall conditions ($T^+ \approx 100$), causing a gradual downstream decay of the drag reduction $DR\%$. The same logic applies to temporally developing boundary layers (TTBLs), as confirmed by Moroni et al. (2026), where spatial downstream development is substituted by temporal evolution over time t. Figures 4.5, 4.6 and 4.4 illustrate the temporal evolution of inner-scaled parameters for both OW and STW cases, showing consistency with the expected behaviour.

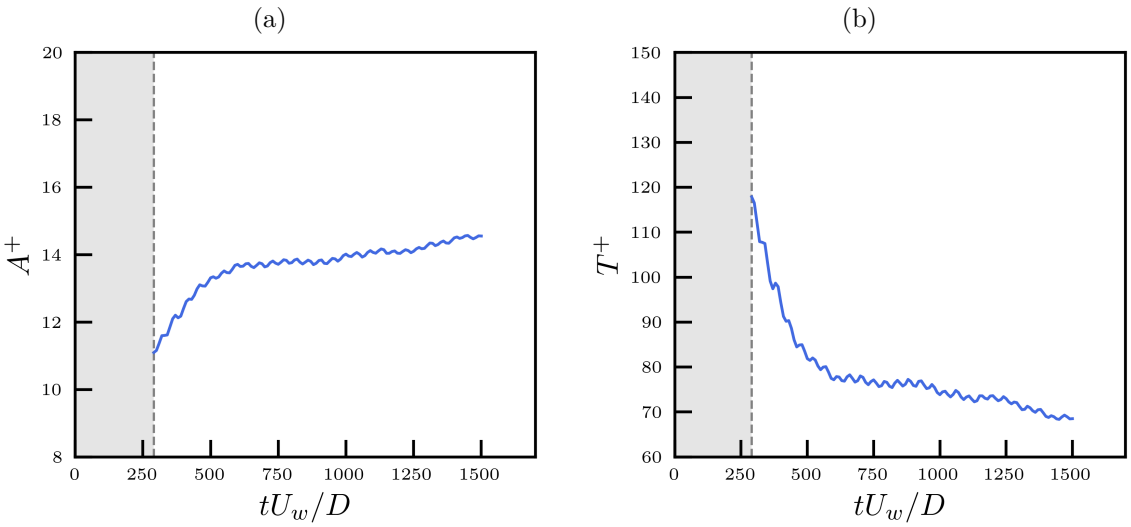


Figure 4.4: OW parameters, expressed in inner units. (a) A^+; (b) T^+. Grey rectangle represents transient time interval of initial condition and onset of wall oscillations.

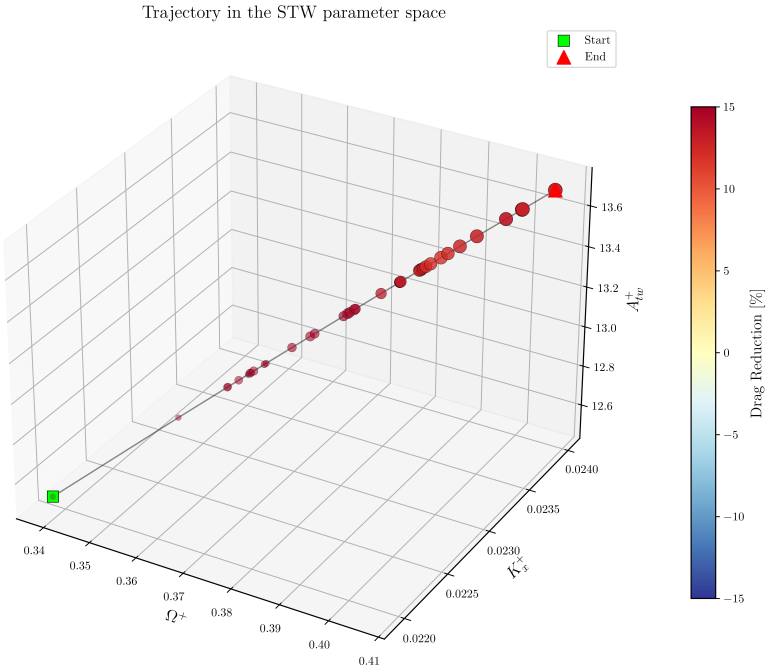


Figure 4.5: STW parameter trajectory in 3D space. Amplitude, wavelength and frequency, expressed in inner units, grow due to friction velocity decay in time; TW-DR case.

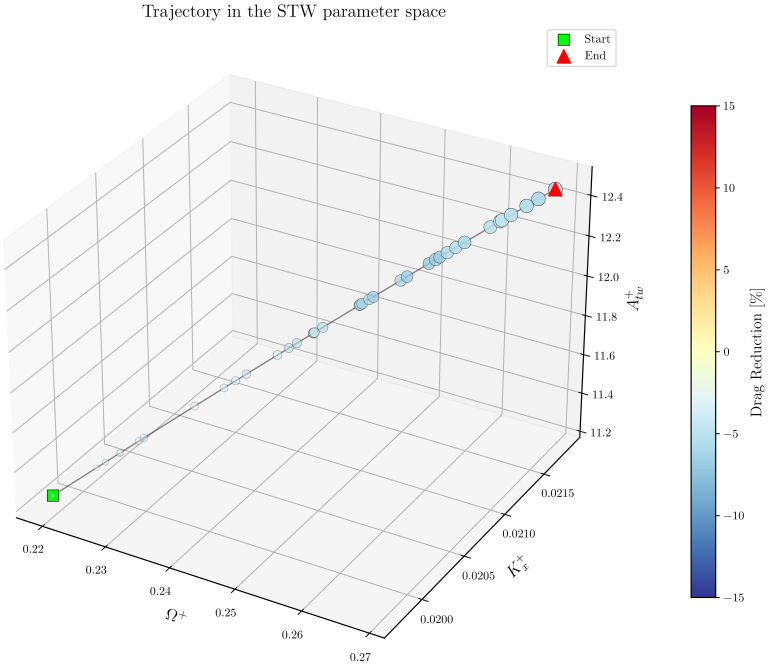


Figure 4.6: STW parameter trajectory in 3D space. Amplitude, wavelength and frequency, expressed in inner units, grow due to friction velocity decay in time; TW-DI case.

Chapter 5

Results

In this chapter, results from all simulated cases are presented and discussed. First, a general overview of the flow cases is provided, highlighting the main differences in terms of flow control strategies and adverse pressure gradient conditions. Then, the effects of spanwise wall forcing on the boundary layer under pressure gradient are analyzed, followed by streamwise traveling waves alike analysis.

5.1 Simulated cases/overview

Flow Case	A/U_w	TU_w/D	A_0^+	T_0^+	k	λ_x	c^+	$t_{0,apg}U_w/D$
FW	0	∞	0	∞	/	/	/	/
OW	0.5678	90	12	100	/	/	/	/
APG	0	∞	0	∞	/	/	/	650
OW-APG	0.5678	90	12	100	/	/	/	650
TW-DR	0.5678	18	12	20	4.9754	12.6286	≈ 15	/
TW-DI	0.5678	22.5	12	25	4.9754	12.6286	≈ 12	/
TW-DR-APG	0.5678	18	12	20	4.9754	12.6286	≈ 15	362
TW-DI-APG	0.5678	22.5	12	25	4.9754	12.6286	≈ 12	380

Table 5.1: Flow cases simulated with corresponding flow control strategy parameters. The time $t_{0,apg}$ indicates when the adverse pressure gradient is activated, following 5.2. Values of k and w are derived from Figure 2. of Quadrio et al. (2009) and scaled to the TBL length and velocity reference scales. k and λ_x are expressed in code units (TTBL)

In this section, the specific flow cases simulated in the present work are described in detail, highlighting the variations in flow control strategies and adverse pressure gradient conditions.
Simulations involving spanwise flow control (spanwise oscillations (OW) and streamwise traveling waves (TW)) share a similar set up where the forcing is activated as

soon as the transient following Kozul et al. (2016)'s initial conditions is over. This occurs when $Re_\theta = Re_D = 500$, to which a friction Reynolds number $Re_\tau \approx 200$ corresponds, reached at time unit $tU_w/D = 290$.

$$t_{start,ow} = t_{start,tw} = 290 \qquad Re_{\tau,0} = 200 \tag{5.1}$$

The adverse pressure gradient, instead, is activated at a later time unit, after the transient of the wall forcing is over. This is expected to occur four periods after the forcing is activated. Therefore:

$$t_{start,apg} = t_{start,ow} + 4t_{ow} \tag{5.2}$$

where t_{ow} is the period of the spanwise wall oscillation. The same applies to traveling waves cases.

Flow Case	Re_τ	Re_τ *interval*	Re_θ	$(t_1 - t_2)U_w/D$	$10^3\langle cf \rangle$	Δx^+	$\Delta {y_w}^+$	$\Delta {y_d}^+$	Δz^+
FW	303	(203.3 ÷ 337.9)	694.0	(300 ÷ 700)	4.781	16.88	0.26	3.26	8.44
FW	424	(337.9 ÷ 474.3)	1058.0	(700 ÷ 1200)	4.254	15.93	0.24	4.43	7.96
FW	533	(528.5 ÷ 544.5)	1435.0	(1417.5 ÷ 1500)	3.96	15.36	0.24	6.94	7.68
OW	429	(420.3 ÷ 433.8)	1246.0	(1417.5 ÷ 1500)	3.057	13.5	0.21	5.2	6.75
APG	281	(295.4 ÷ 254.4)	10757.0	(1230 ÷ 1312.5)	0.86	7.16	0.11	3.93	3.58
OW-APG	219	(240.9 ÷ 189.8)	10784.0	(1230 ÷ 1312.5)	0.469	5.29	0.08	3.22	2.64
TW-DR	455	(455.4 ÷ 453.8)	1269.0	(1483.5 ÷ 1500)	3.429	14.3	0.22	5.51	7.15
TW-DI	519	(518.7 ÷ 513.6)	1429.0	(1477.5 ÷ 1500)	4.159	15.75	0.24	6.49	7.87
TW-DR-APG	/	/	/	(1483.5 ÷ 1500)	/	/	/	/	/
TW-DI-APG	/	/	/	(1477.5 ÷ 1500)	/	/	/	/	/

Table 5.2: Simulation details for second-order statistics calculated over a time period, TU_w/D, centered in time around the target Re_τ. Re_τ interval and the corresponding time unit interval are reported, as well as the momentum thickness Reynolds number Re_θ at the center of the time interval. Friction coefficient cf and numerical resolution are reported, with Δy_w^+ refers to the first element at the wall and Δy_d^+ refers to the element at the boundary layer thickness.

5.2 TTBL under adverse pressure gradient with spanwise oscillating wall forcing

Given that the purpose of this work is to evaluate whether spanwise forcing promotes or delays separation, the results from the purely OW and APG-subjected cases will be only briefly discussed, since both frameworks were previously validated by Moroni et al. (2026) and Cesari (2026). The focus will be on the combined OW-APG, TW-APG cases, which represents the main novelty of this work, together with the purely TW cases which only recently have been implemented on the Incompact3d code.

5.2.1 Time evolution and flow quantities

Figure 5.1 shows the time evolution of the main flow quantities for the OW and APG-subjected cases.

Consistently with previous results in temporal TBLs Moroni et al. (2026), spanwise wall oscillations significantly reduce the skin-friction coefficient c_f with respect to the uncontrolled FW case, although the drag reduction $R\%$ decreases slightly in time. The control also limits the growth of the boundary layer thickness δ_{99}, and the difference between OW and FW increases with time despite the slow decay of $R\%$. Since both c_f and δ_{99} are reduced, Re_τ is also lower in the OW case. When plotted against Re_θ, the c_f reduction remains evident while the Re_τ deviation is much milder, suggesting that the overall dynamics is not strongly affected by the control.

In the APG case, the results agree well with Cesari (2026) and capture the behaviour expected in APG-subjected turbulent boundary layers. After the activation of the forcing, c_f decreases steeply, confirming that the chosen forcing magnitude drives the flow to incipient separation, which is reached at the end of the simulation. The thickness δ_{99} grows monotonically owing to the accumulation of decelerated, low-momentum fluid. This growth initially counteracts the drop in skin friction, but the decay of the friction velocity eventually dominates, and Re_τ decreases.

When the APG is applied to the OW flow, the skin friction has already been reduced with respect to the uncontrolled case, as a consequence of the attenuation of near-wall turbulent stresses. The APG thus acts on a boundary layer whose ability to replenish near-wall momentum is already weakened, which makes it more susceptible to the imposed deceleration and favours an earlier approach to separation.

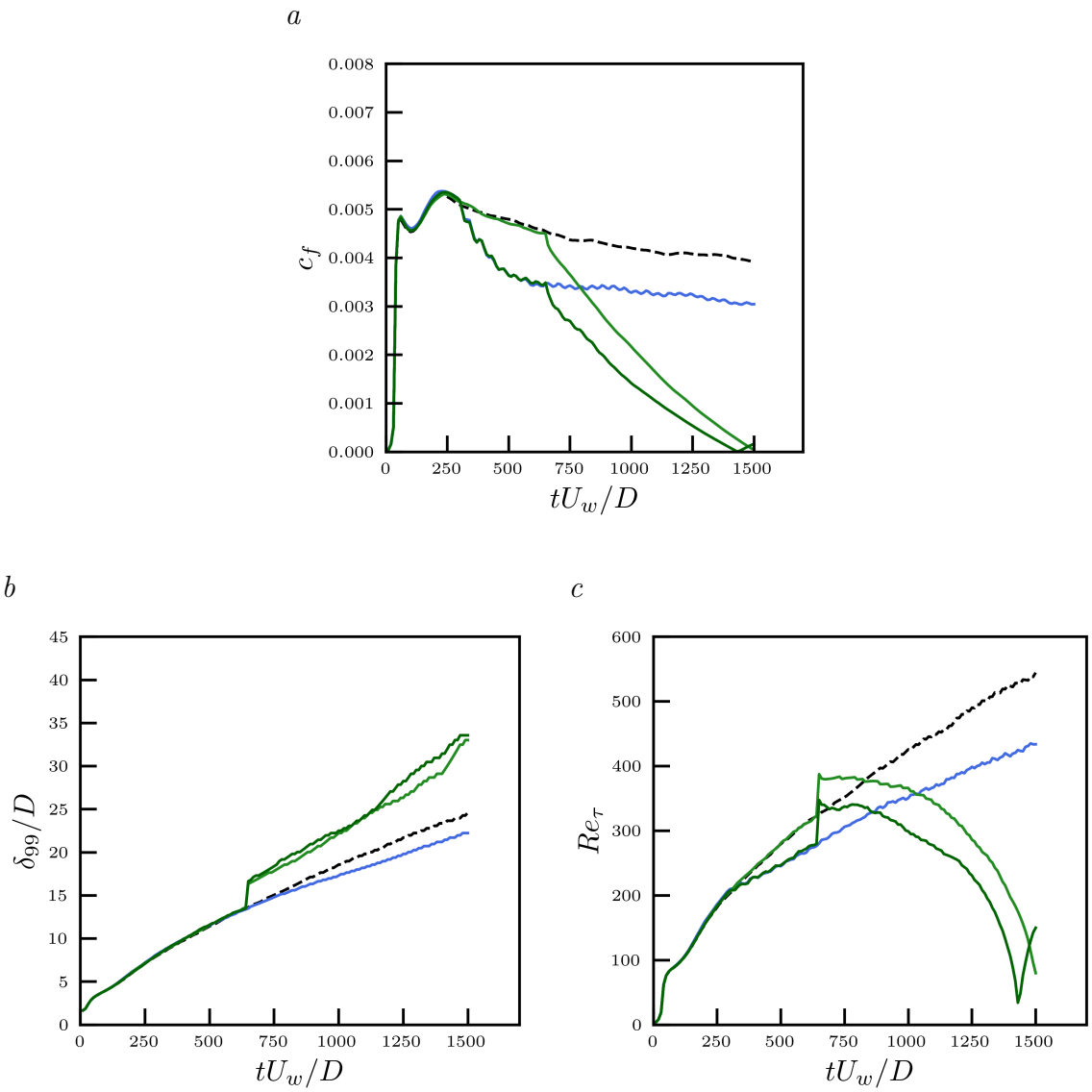


Figure 5.1: Time evolution quantities comparison for all OW and APG-subjected cases. (a) Skin friction coefficient c_f; (b) Boundary layer thickness δ_{99}; (c) Friction Reynolds number Re_τ. Black dashed line represents FW; Blue line represents OW; Green line represents APG; Drakgreen line represents OW-APG.

Compared to the uncontrolled APG case, the OW-APG case shows only a slightly larger δ_{99}. The distinctive feature is instead the steeper decay of c_f after the APG activation in 5.1a, which brings the flow to low friction values earlier. Since Re_τ is linked to the friction velocity, its lower value in OW-APG, already present before the APG because of the control, is further reduced by this faster drop of c_f. The Re_τ reduction is therefore mainly due to the steeper decrease of skin friction rather than to a different boundary layer growth.

Overall, the wall oscillation does not modify the pressure-gradient-driven evolution of the mean flow, as shown by the same H–Re_θ trajectory, but changes the state of the

near-wall turbulence on which the APG acts. The earlier promotion of separation is thus consistent with a history effect of the forcing on the response of turbulence to the adverse pressure gradient.

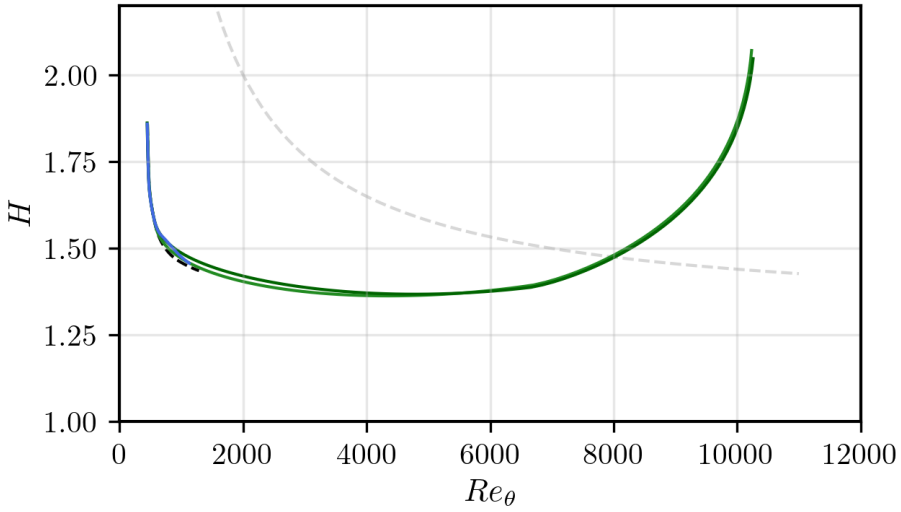


Figure 5.2: Momentum thickness shape factor H vs momentum thickness Reynolds number Re_θ for all OW and APG-subjected cases. Black dashed line represents FW; Blue line represents OW; Green line represents APG; Drakgreen line represents OW-APG.

5.2.2 Mean velocity profiles

The analysis of the mean velocity profiles highlights the different physical mechanisms through which near-wall active forcing and external deceleration reshape the boundary layer structure. It is to acknowledge that this is not a comparison across the three simulations, since the friction Reynolds number is different in each case, and each case is compared to the uncontrolled FW case at a respectively similar friction Reynolds number. The comparison is rather intended to highlight the different effects of the two forcing mechanisms on the mean flow.

Starting with the OW case, figure 5.3, the mean velocity profile reveals a localized thickening and upward displacement within the viscous sublayer and buffer region. As widely established in literature, the unsteady shear layer generated by the wall oscillation (Stokes layer) alters the near-wall dynamics, forcing the canonical Self-Sustaining Process (SSP) to lift off and reorganize further away from the wall. In external scaling (y/D), the profile collapses almost perfectly onto the unforced baseline in the outer region ($y/D > 0.2$), confirming that the control remains strictly confined to the viscous layer while slightly reducing the near-wall velocity gradient. In the APG case, figure 5.4, under external deceleration, the flow dynamic shifts to-

ward the outer layer. The volumetric pressure gradient flattens the near-wall velocity gradient while inducing a severe momentum deficit that thickens the mean profile predominantly in the wake region. When viewed in outer units, the profile clearly highlights the pronounced momentum depletion, where the external deceleration flattens the near-wall velocity U/U_w.

In the combined OW-APG setup, figure 5.5, the physical mechanisms of both forcings superimpose. The wall oscillation first induces a structural displacement of the velocity profile near the wall via the Stokes layer. Subsequently, the adverse pressure gradient acts upon this pre-conditioned state, further expanding the momentum deficit in the wake region. Because the near-wall turbulence is already lifted and restructured by OW prior to the full development of the APG, the velocity profile undergoes a smooth, continuous displacement across both inner and outer regions, accelerating the overall depletion of near-wall momentum. Outer scaling with y/δ_{99} shows to well replicate what discussed above and displays a curious insight that will be discussed in the following Chapter 6.

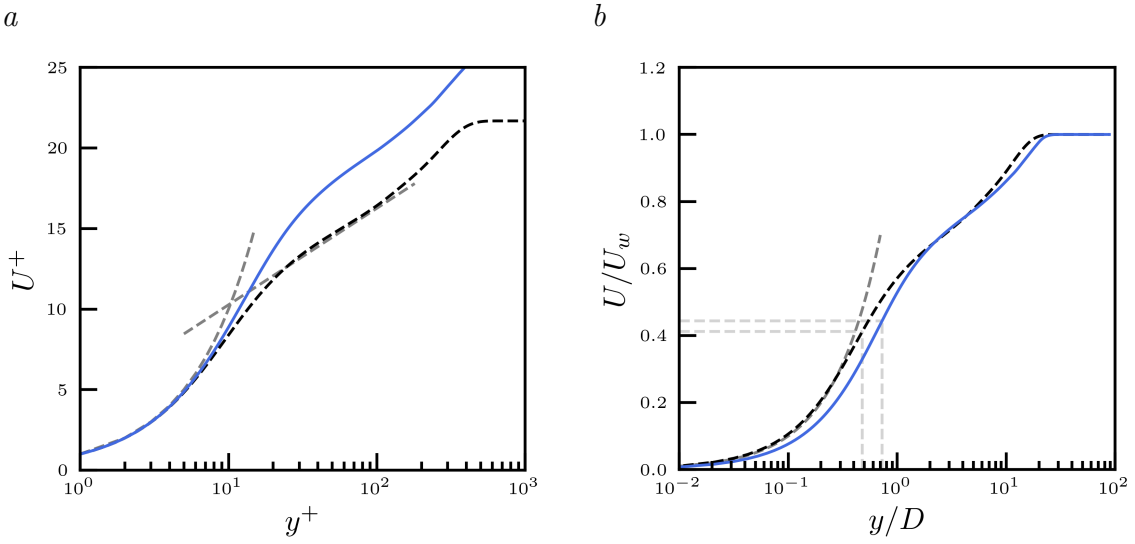


Figure 5.3: Mean velocity profiles for OW case. (a) Inner scaling; (b) external scaling.

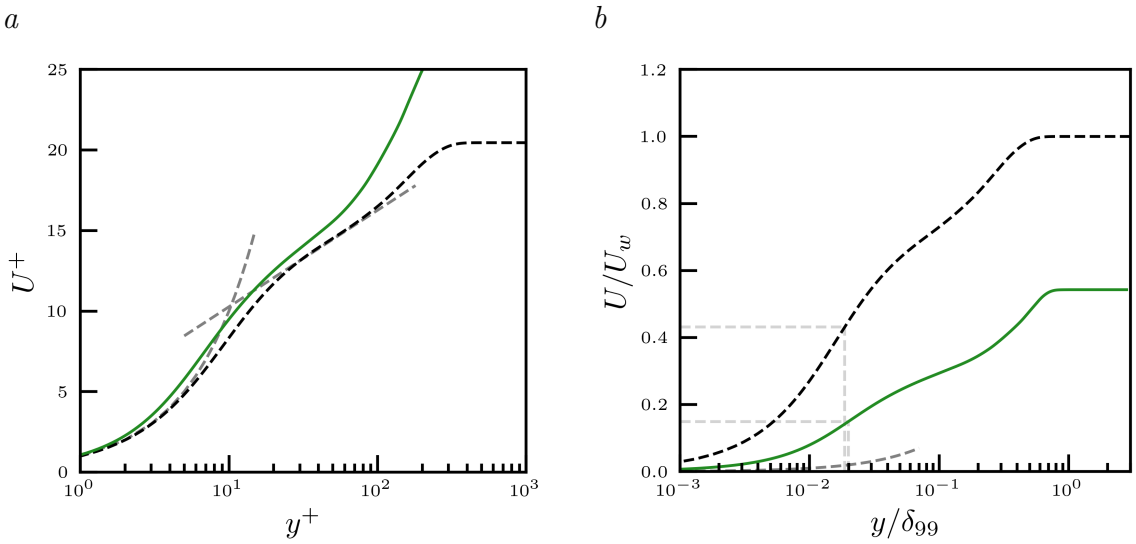


Figure 5.4: Mean velocity profiles for APG case. (a) Inner scaling; (b) outer scaling.

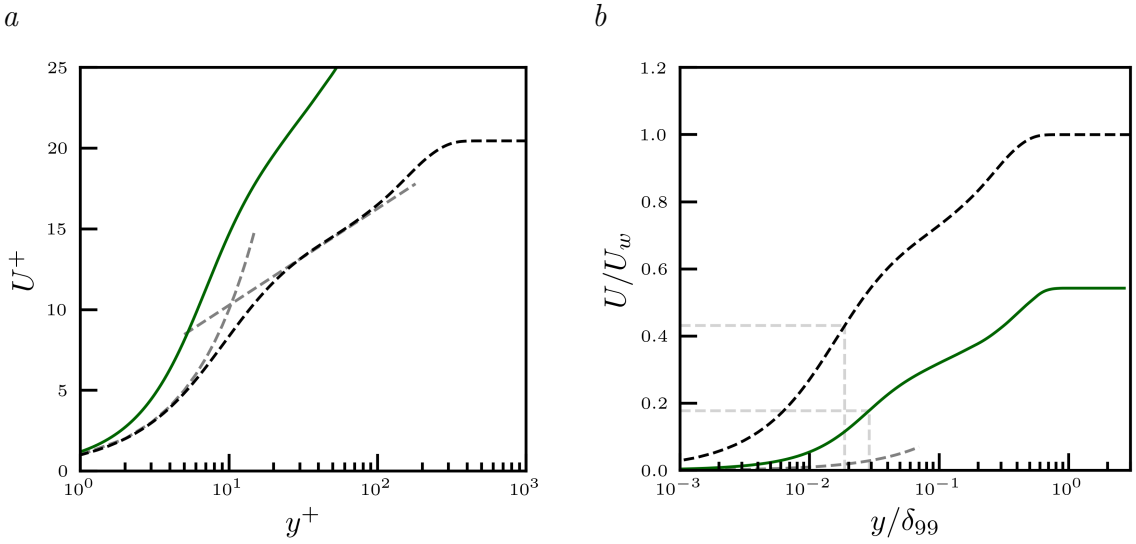


Figure 5.5: Mean velocity profiles for OW-APG case. (a) Inner scaling; (b) outer scaling.

5.2.3 Second-order statistics

Second-order statistics of TTBLs with wall oscillations are reported in figures 5.6 and 5.7. Results are consistent with those of Moroni et al. (2026), confirming a mild shift of all profiles towards higher y^+. This outward displacement is also evident in the mean velocity profile through an upward shift (ΔB^+), illustrated in figure 5.5a . By confining its unsteady transverse shear to $y^+ < 15\breve{}20$, the Stokes layer disrupts streak coherence and thickens the viscous sublayer, forcing the autonomous self-sustaining cycle of turbulence to reorganize further away from the wall.
Moreover, a reduction of the peak of $\langle u'^2 \rangle$ is observed, conversely to those of the

other statistics which remain almost unchanged.
In external scaling, consistently with Moroni et al. (2026), all second-order statistics are reduced, and a more pronounced shift towards the outer region is observed when compared to the uncontrolled FW case.
While the suitability and accuracy of the temporal TTBL formulation under adverse pressure gradients were already validated by Cesari (2026), the present and direct comparison confirms and reinforces the employment of this methodology. The uncontrolled APG flow at $Re_\tau = 281$ ($dP_e/dx = 0.000736$) is directly compared to the uncontrolled (FW) Zero Pressure Gradient baseline at a similar friction Reynolds number ($Re_\tau = 303$). The comparison shown in figures 5.8 and 5.9 reveals three fundamental physical transformations induced by the adverse pressure gradient:

1. Outward Shift of Turbulent Activity: In the uncontrolled FW baseline regime, the maximum turbulent shear stress resides near the wall, reflecting the dominance of near-wall turbulent production within the viscous sublayer. Under APG conditions, fluid deceleration causes the region of primary turbulent activity to detach from the wall and shift outward into the outer layer.

2. Emergence of a Second Outer Peak: As the adverse pressure gradient decelerates the near-wall flow, the mean wall shear stress (τ_w) drops, diminishing the relative contribution of the small-scale viscous near-wall structures. Concurrently, the pronounced fluid deceleration causes a rapid thickening of the boundary layer (δ_{99}), displacing the primary region of turbulence production away from the wall. Within this expanded outer region, large-scale turbulent structures become highly energetic and dominant, driving strong momentum mixing that statistically manifests as a prominent outer peak in the Reynolds stress profiles and streamwise velocity variance.

3. Amplification of Turbulent Fluctuations: The global fluid deceleration imposed by the volumetric momentum forcing ($dP_e/dx = 0.000736$) causes the thickening of the boundary layer and the depletion of the near-wall mean velocity, significantly amplifying the magnitude of turbulent velocity fluctuations and momentum transport.

These results reinforce the temporal APG framework validated by Cesari (2026) and align with the canonical spatial DNS of Kitsios et al. (2016) and Kitsios et al. (2017). Furthermore they confirm that, despite the presence of non-self-similar history effects, the temporal TTBL framework accurately reproduces the essential physical mechanisms of APG boundary layers.

As shown in figures 5.10 and 5.11, in contrast to the uncontrolled APG baseline—which exhibits a characteristic double-peak structure representing the coexistence of residual near-wall turbulent production and outer momentum transport induced by flow deceleration—the combined OW-APG configuration displays only a single, broadened outer peak. This difference stems from the initial pre-conditioning of the boundary layer by the oscillating wall. The unsteady Stokes layer generated by OW lifts and shifts the near-wall turbulent activity away from the wall prior to the full development of the pressure gradient. As a result, the canonical near-wall peak ($y^+ \approx 15$) is no longer present as a distinct feature. When the adverse pressure gradient takes effect, instead, the turbulent fluctuations and Reynolds stresses merge into a single, smooth outer peak that is displaced further away from the wall while maintaining the overall shape of the baseline profile. the outward shift and the amplification of turbulent fluctuations are fully recovered, as evidenced by figures 5.10 and 5.11. This behavior stems from the fact that the superposition of wall oscillations and external deceleration induces a more severe momentum deficit and a slightly higher boundary layer thickness (δ_{99}) compared to the uncontrolled APG baseline. This expansion shifts the core turbulent activity further away from the wall, engaging larger-scale turbulent structures in the wake region and intensifying momentum transport in the outer layer. This outer-layer energization is directly consistent with the accelerated depletion of near-wall momentum, which promotes earlier separation as observed in the temporal evolution of c_f and Re_τ.

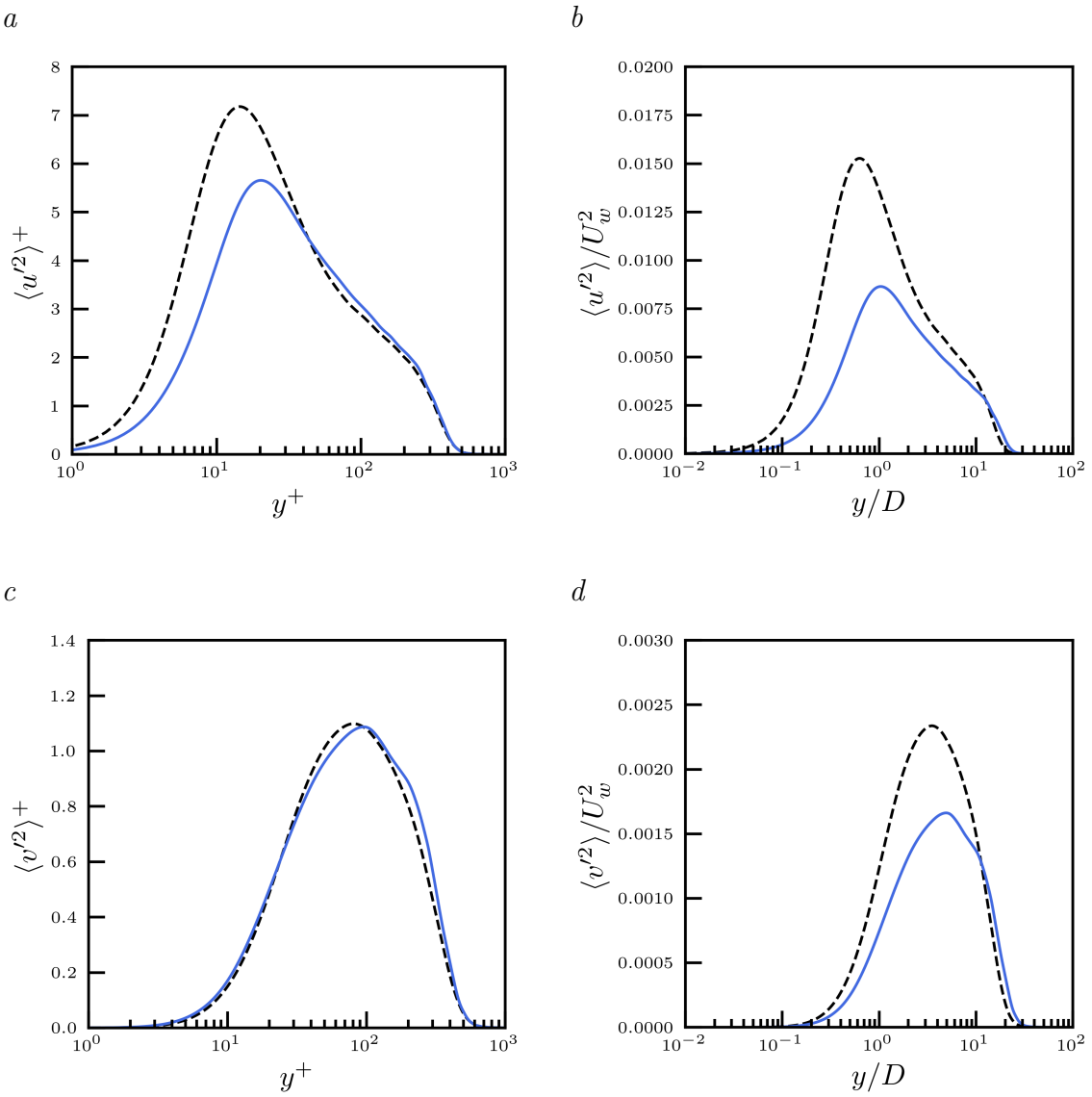


Figure 5.6: FW and OW cases comparison. Black dashed line represents FW at $Re_\tau = 424$; Blue line represents OW at $Re_\tau = 429$. (a,b) Streamwise velocity variance; (c,d) Wall-normal velocity variance. Left column (a,c) shows inner scaling through actual friction velocity; right column (b,d) shows external scaling with trip wire diameter D and wall velocity U_w.

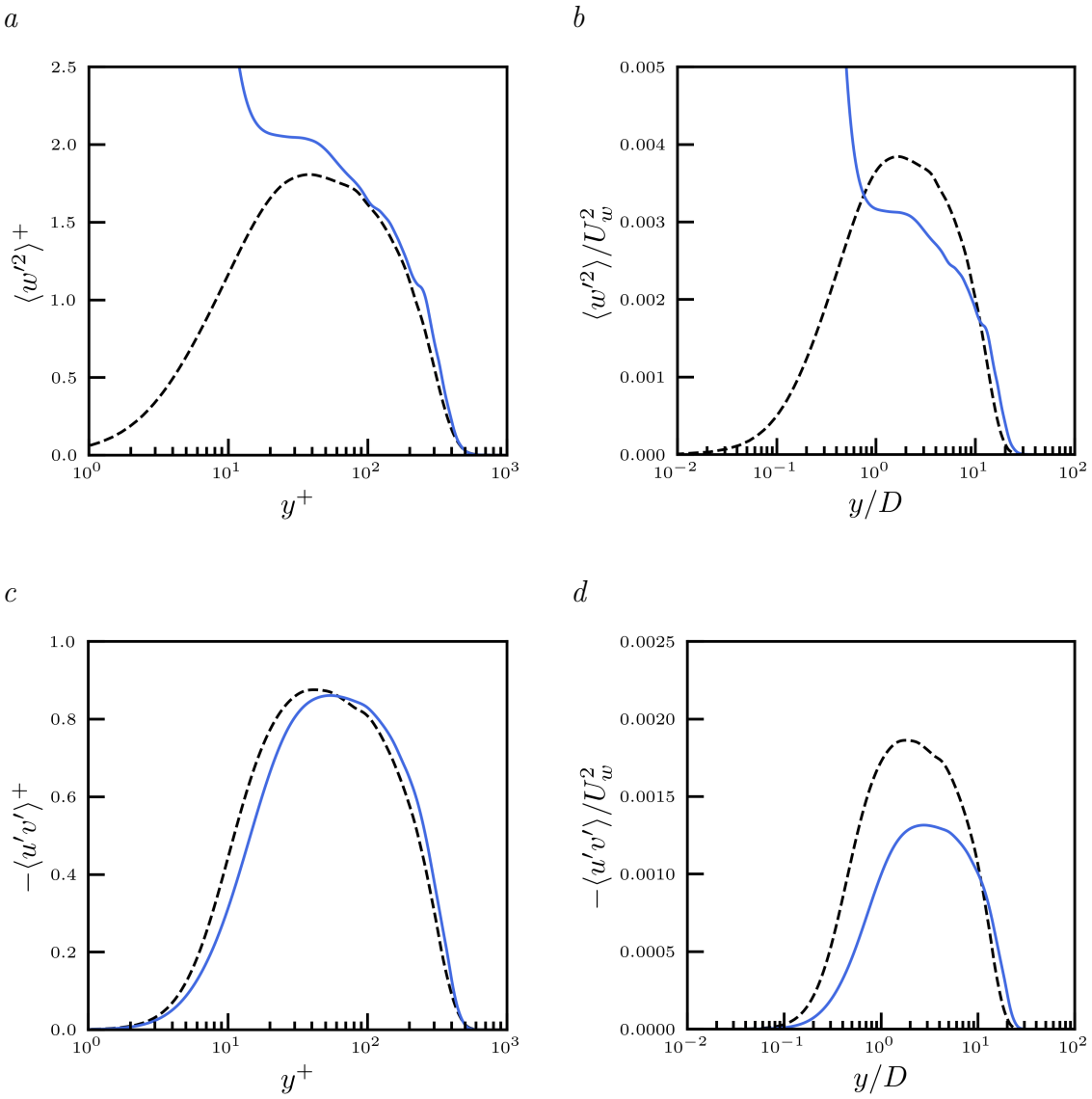


Figure 5.7: FW and OW cases comparison. Black dashed line represents FW at $Re_\tau = 424$; Blue line represents OW at $Re_\tau = 429$. (a,b) Spanwise velocity variance; (c,d) Reynolds stress. Left column (a,c) shows inner scaling through actual friction velocity; right column (b,d) shows external scaling with trip wire diameter D and wall velocity U_w.

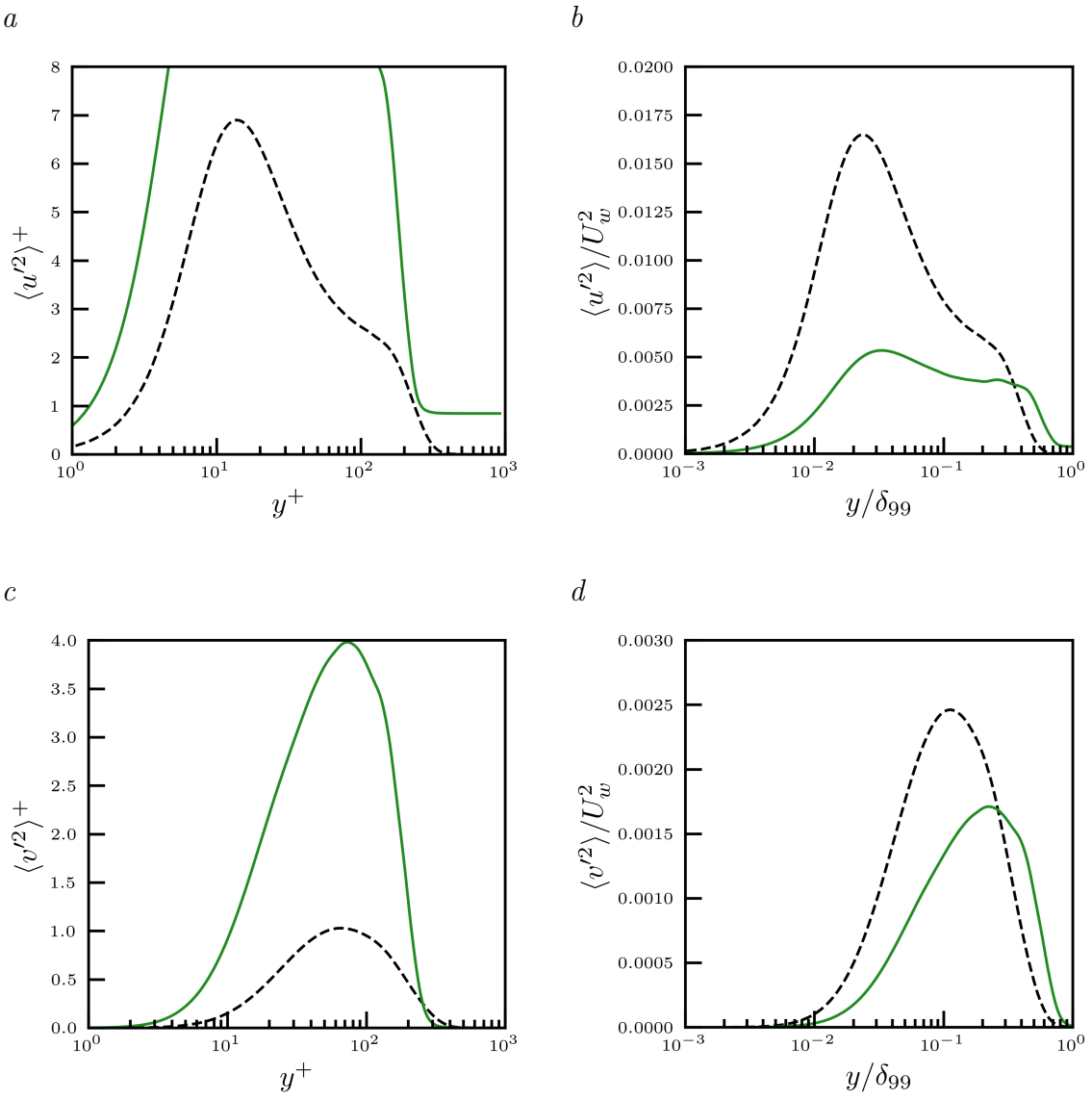


Figure 5.8: FW and APG cases comparison. Black dashed line represents FW at $Re_\tau = 303$; Green line represents APG at $Re_\tau = 281$. (a,b) Streamwise velocity variance; (c,d) Wall-normal velocity variance. Left column (a,c) shows inner scaling through actual friction velocity; right column (b,d) shows outer scaling.

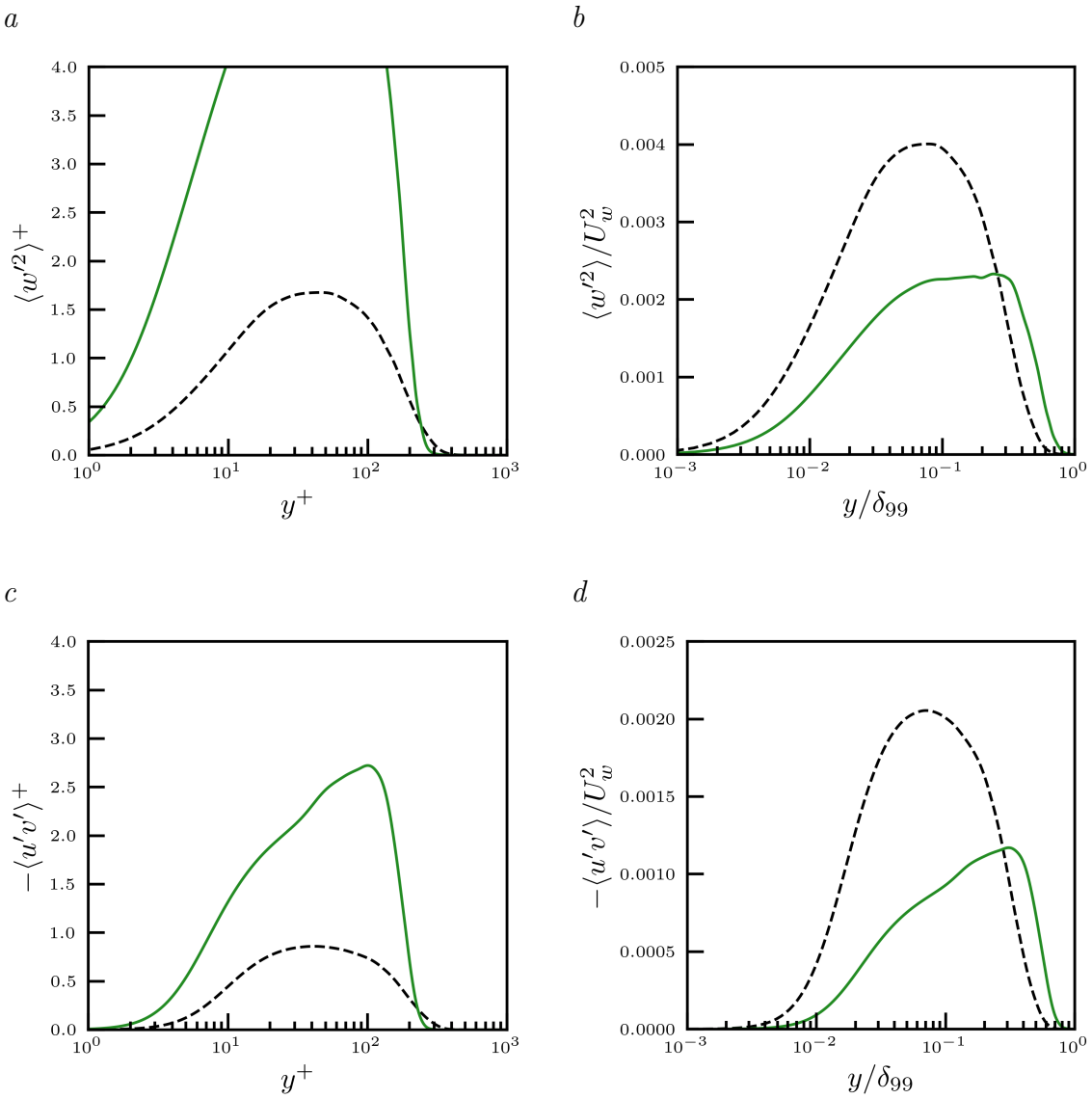


Figure 5.9: FW and APG cases comparison. Black dashed line represents FW at $Re_\tau = 303$; Green line represents APG at $Re_\tau = 281$. (a,b) Spanwise velocity variance; (c,d) Reynolds stress. Left column (a,c) shows inner scaling through actual friction velocity; right column (b,d) shows outer scaling.

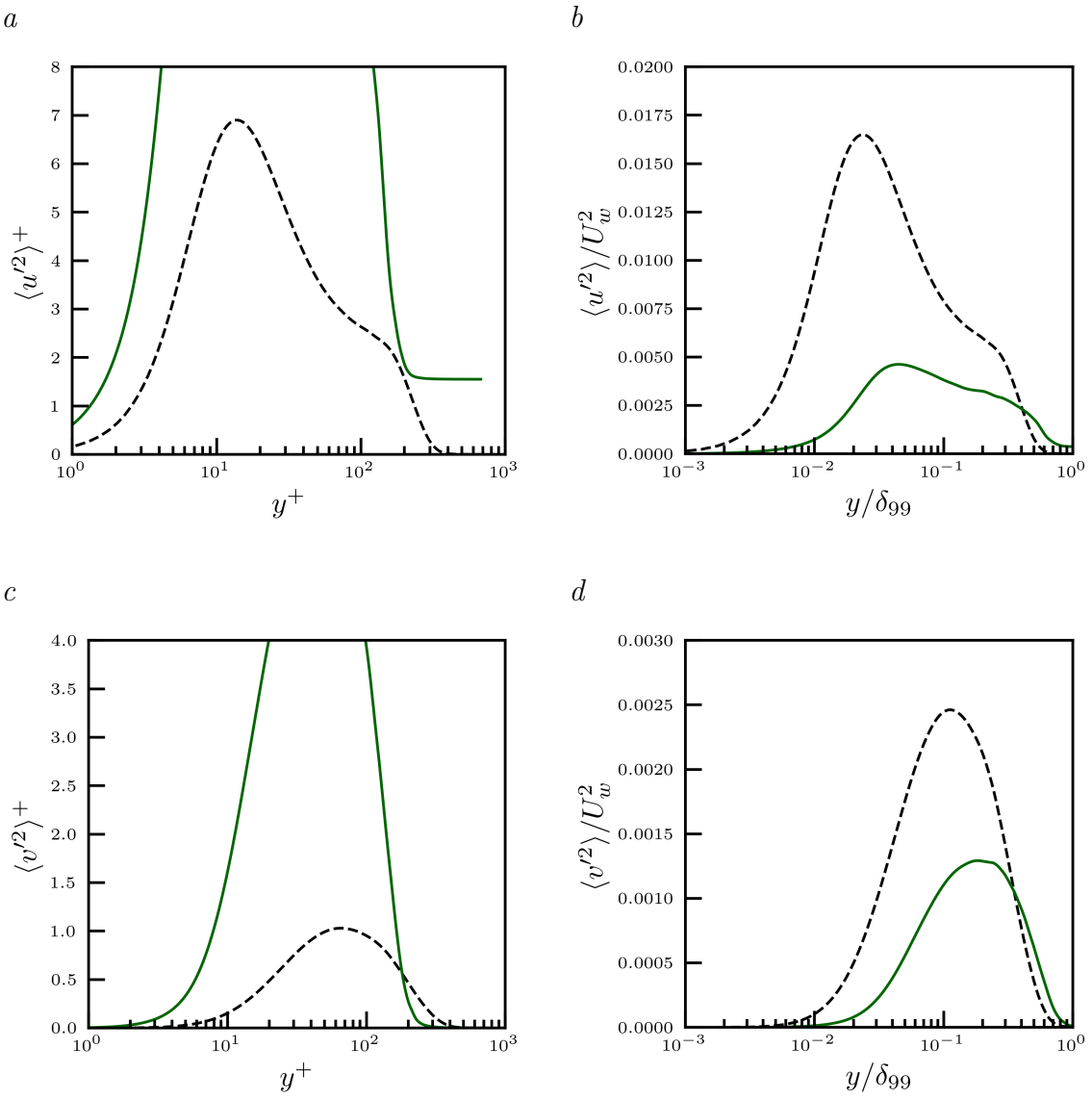


Figure 5.10: FW and APG cases comparison. Black dashed line represents FW at $Re_\tau = 303$; Dark green line represents OW-APG at $Re_\tau = 219$. (a,b) Streamwise velocity variance; (c,d) Wall-normal velocity variance. Left column (a,c) shows inner scaling through actual friction velocity; right column (b,d) shows outer scaling.

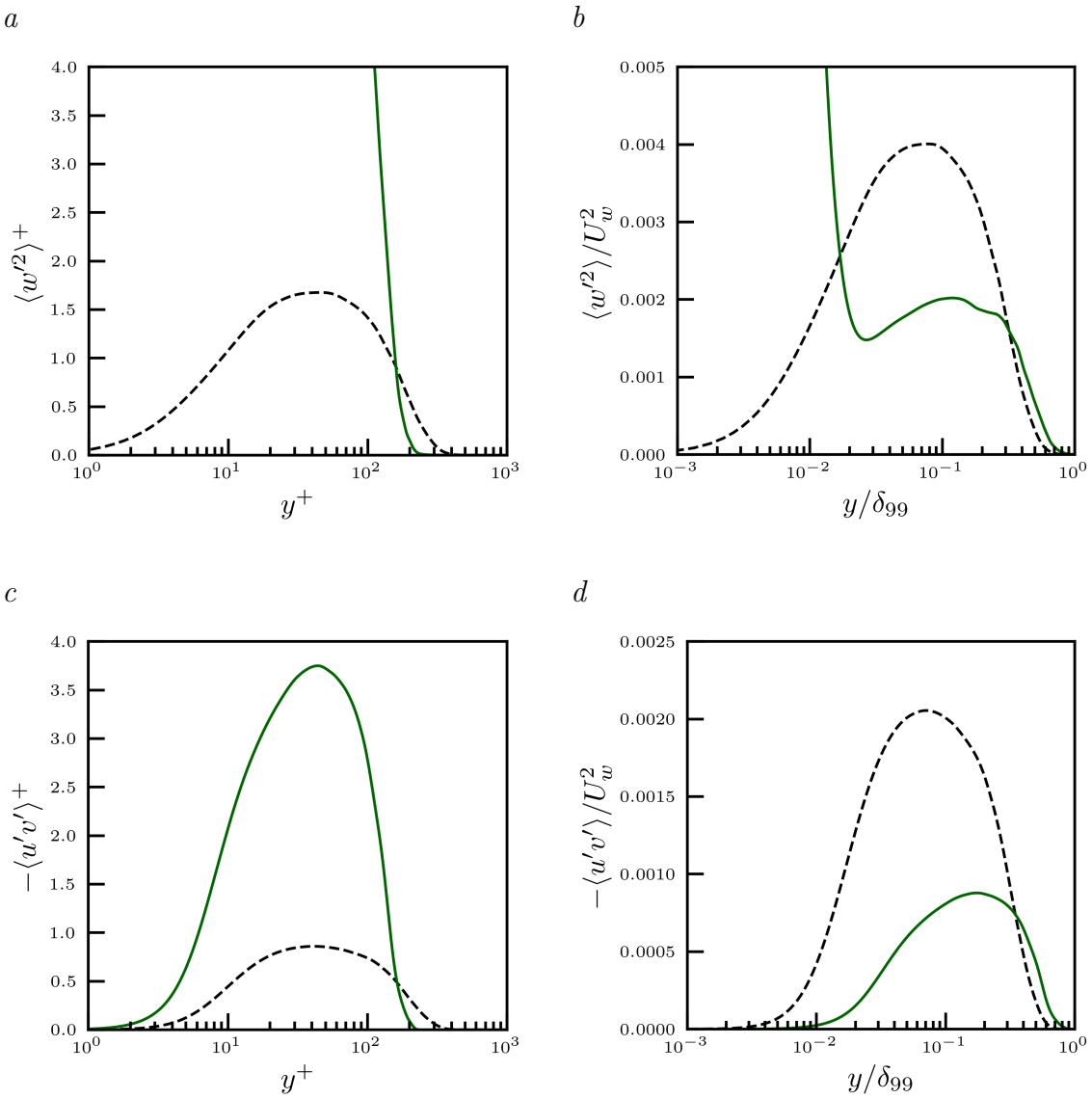


Figure 5.11: OW and APG cases comparison. Black dashed line represents OW at $Re_\tau = 219$; Dark green line represents OW-APG at $Re_\tau = 219$. (a,b) Spanwise velocity variance; (c,d) Reynolds stress. Left column (a,c) shows inner scaling through actual friction velocity; right column (b,d) shows outer scaling.

5.3 TTBL under adverse pressure gradient with streamwise traveling wave forcing

In this section, results from the TW cases will be discussed, with a focus on the combined TW-APG cases. Dual-regime, DR and DI, comparison is maintained throughout the analysis with the aim to provide a complete picture of how wave-turbulence interactions affect the response of the boundary layer and influence separation.

5.4 Time evolution and flow quantities

Figure 5.12 shows the time evolution of the main flow quantities for all TW and APG-subjected cases.
For the TW-DR case, the time evolution of c_f, δ_{99} and Re_τ is consistent with the OW case, confirming that the drag reduction regime is characterized by a reduction of skin friction and a slower growth of the boundary layer thickness. The TW-DI case shows a slight increase of the friction coefficient cf, milder than the one observed by Quadrio et al. (2009) at the same corresponding values of k and w. This difference is likely due to the different friction Reynolds number, flow case and the temporal nature of the present simulations. Boundary layer thickness δ_{99} and friction Reynolds number Re_τ almost replicate the uncontrolled FW case, thus being slightly lower, as a consequence of the mild drag increase.
When the APG is applied to the TW cases, the skin friction decreases steeply after the APG activation, similar to the OW-APG case, showing, again, that the chosen forcing magnitude drives the flow to separation. Boundary layer thickness and friction Reynolds number also well replicate the behaviour of OW-APG case.

As stated by equation 5.2, adverse pressure gradient activation is set four oscillating periods after the onset of the forcing. However, owing to the smaller oscillating periods-chosen to allow the dual-regime comparison-the onset of the adverse pressure gradient is different in each case. In particular, in TW-DR-APG case the pressure gradient onset is set to occur earlier than in the TW-DI-APG case, respectively at $tU_w/D = 362$ and $tU_w/D = 380$. Moreover, due to this earlier onsets with respect to the OW-APG case, it is more difficult to assess whether streamwise traveling waves drive the flow to separation earlier than wall oscillations and allow a direct comparison between the two forcings. This can be done only qualitatively, by comparing each case's time interval, from the onset of the pressure gradient to separation, with the corresponding time interval of the purely APG case.

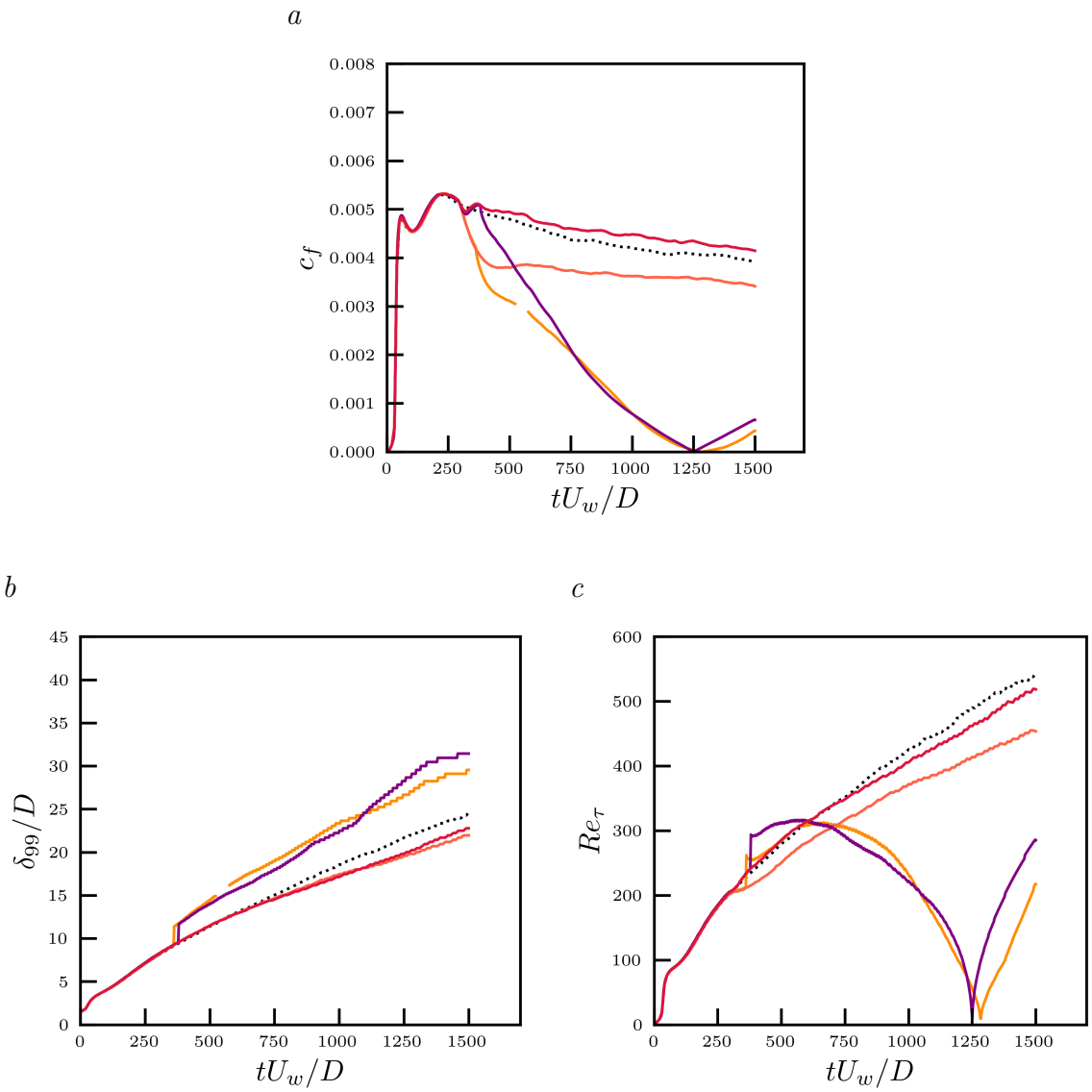


Figure 5.12: Time evolution quantities comparison for all TW and APG-subjected cases. (a) Skin friction coefficient c_f; (b) Boundary layer thickness δ_{99}; (c) Friction Reynolds number Re_τ. Black dashed line represents FW; Red line represents TW-DR; Magenta line represents TW-DI; Orange line represents TW-DR-APG; Purple line represents TW-DI-APG.

Separation occurs at $t = 1430$ in the OW-APG case against $t = 1500$ in the uncontrolled case: the oscillation anticipates it by 70 time units, i.e. by about 8% of the interval between activation and separation (Table 5.3). The TW-DR-APG case separates 918 time units after the activation, about 8% later than the uncontrolled case, whereas the TW-DI-APG case separates after 870 time units, a difference of about 2% that lies within the uncertainty on the determination of t_{sep}. The OW and the TW-DR cases both reduce the skin friction, yet they have opposite effects on the onset of separation, which suggests that the amount of drag reduction alone does

not determine the response of the boundary layer to the pressure gradient. These TW results are preliminary and a more accurate analysis is left for future work.

Case	t_{onset}	t_{sep}	Δt_{sep}	$\Delta t_{sep}/\Delta t_{sep}^{APG}$
APG	650	1500	850	1
OW-APG	650	1430	780	0.917
TW-DR-APG	362	1280	918	1.08
TW-DI-APG	380	1250	870	1.02

Table 5.3: Activation time of the pressure gradient, separation time ($c_f = 0$) and time elapsed between the two, in units of tU_w/D.

5.5 Mean velocity profiles

Mean streamwise velocity profile U^+ macroscopically reflects the structural reorganization of the near-wall layer under traveling-wave actuation. Figure 5.13 shows mean velocity profiles of TW-DR (left side) and TW-DI (right side) cases, compared to the uncontrolled FW case at a similar friction Reynolds number.

Figure 5.13b, corresponding to the TW-DI case, shows a slight downward displacement of the mean velocity profile, which is consistent with the mild drag increase observed in figure 5.12a. Conversely, figure 5.13a, corresponding to the TW-DR case, shows a clear upward shift ($\Delta B > 0$). Remarkably, within the immediate viscous sublayer ($y^+ < 15$), the red profile remains virtually superimposed on the uncontrolled baseline. The upward displacement develops progressively, becoming prominent in the logarithmic and outer regions ($y^+ > 30$–100).

This structural behavior in TW-DR seems to indicate that traveling waves do not achieve drag reduction by expanding the viscous sublayer near the wall. Instead, as revealed by the local skin-friction (C_f) decomposition in the next chapter, the cross-over distance remains virtually unchanged ($y_{co,TW} \approx y_{co,FW}$), proving that the friction drop is driven by a deep penetration of wave forcing into the outer layer, which weakens the non-viscous turbulent momentum transfer.

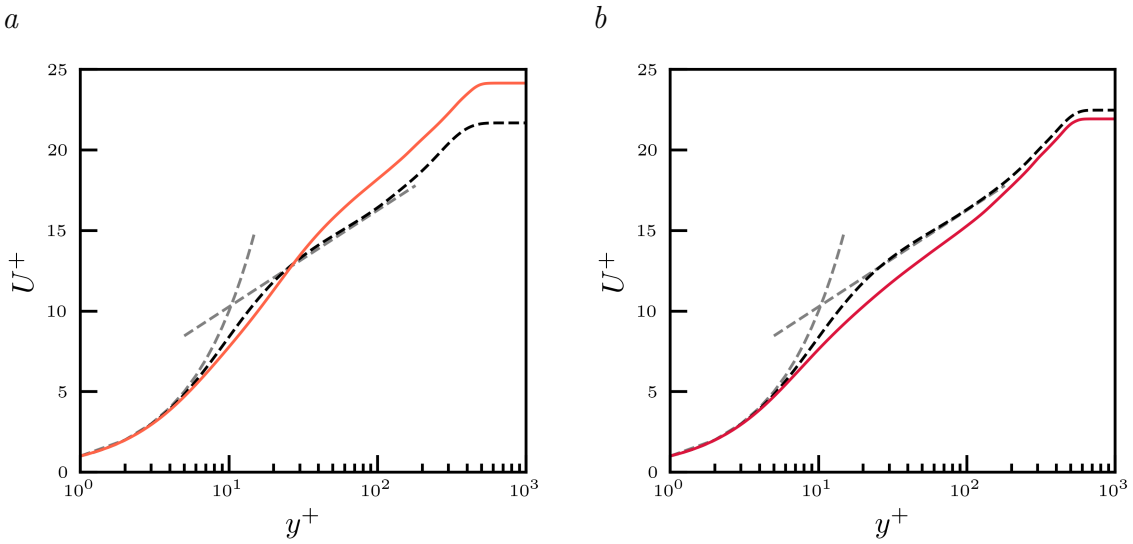


Figure 5.13: Mean velocity profiles for all TW cases. (a) TW-DR, $Re_\tau = 455$; (b) TW-DI, $Re_\tau = 520$

5.6 Second-order statistics

The examination of the second-order turbulent statistics—expressed in both inner and external scaling—provides deeper insight into the physical mechanisms governing the TW-DR and TW-DI regimes.

As shown in figures 5.14 and 5.15, in TW-DI regime, a slight amplification of both the wall-normal velocity variance ($\langle v'^2 \rangle$) and the turbulent shear stress ($-\langle u'v' \rangle$) is observed compared to the uncontrolled baseline (FW). This enhancement is driven by phase-locking resonance between the wave phase speed and the convection velocity of near-wall turbulent structures ($c^+ \approx U_c^+ \approx 10$), which intensifies vertical momentum exchange Quadrio et al. (2009) and Quadrio et al. (2011). Interestingly, despite the rise in $\langle v'^2 \rangle$ and $-\langle u'v' \rangle$, the streamwise ($\langle u'^2 \rangle$) and spanwise ($\langle w'^2 \rangle$) normal stresses exhibit a mild attenuation across both inner and external scaling. This indicates that the resonant wave forcing preferentially channels energy into vertical transport rather than streamwise fluctuations. Furthermore, instead of developing an isolated peak displaced away from the wall, the $\langle v'^2 \rangle$ profile in TW-DI exhibits a distinct inward broadening, reflecting the direct penetration of wave-induced vorticity very close to the boundary ($y^+ < 15$).

In the drag-reducing regime TW-DR, a global attenuation across all Reynolds stress components is observed. This attenuation is particularly evident when statistics are non-dimensionalized using external scaling, demonstrating a widespread damping of turbulent kinetic energy throughout the buffer layer (Skote 2022). Unlike the TW-DI

case, the $\langle v'^2 \rangle$ profile in TW-DR undergoes a subtle inward shift, with suppressed fluctuations tightly confined near the wall.

Comparing these statistical distributions with purely temporal wall oscillations OW highlights a fundamental distinction between the two control modes:

1. Absence of Outer Shift in Traveling Waves: Under temporal wall oscillations (OW), the unsteady Stokes layer penetrates deeper into the buffer and logarithmic regions ($y^+ \approx 20 - 30$), inducing a characteristic outward shift of the fluctuation peaks Ricco et al. (2021). In contrast, streamwise-traveling waves (TW) confine their physical actuation within a thinner Generalized Stokes Layer ($\delta^+ \approx 2.8$), inducing an inward shift or broadening of $\langle v'^2 \rangle$ near the wall while leaving the outer profile ($y/\delta > 0.2$) virtually identical to the FW case Quadrio et al. (2011). This confirms that the flow operates under a strongly suppressed state where the near wall-low momentum ribbon acts as a shield, protecting from outer-layer perturbations.

2. Susceptibility to Flow Separation: From a macroscopic standpoint, the outward displacement of Reynolds stresses observed in OW elevates turbulent momentum exchange in the log layer, effectively altering the outer-layer balance and making the boundary layer more vulnerable to separation. Conversely, the inward confinement observed in STW prevents this outer-layer disruption. This suggests that traveling waves do not "pre-condition" the outer flow toward separation in the manner that temporal wall oscillations do, maintaining a structural response that remains much closer to the uncontrolled flat-wall baseline.

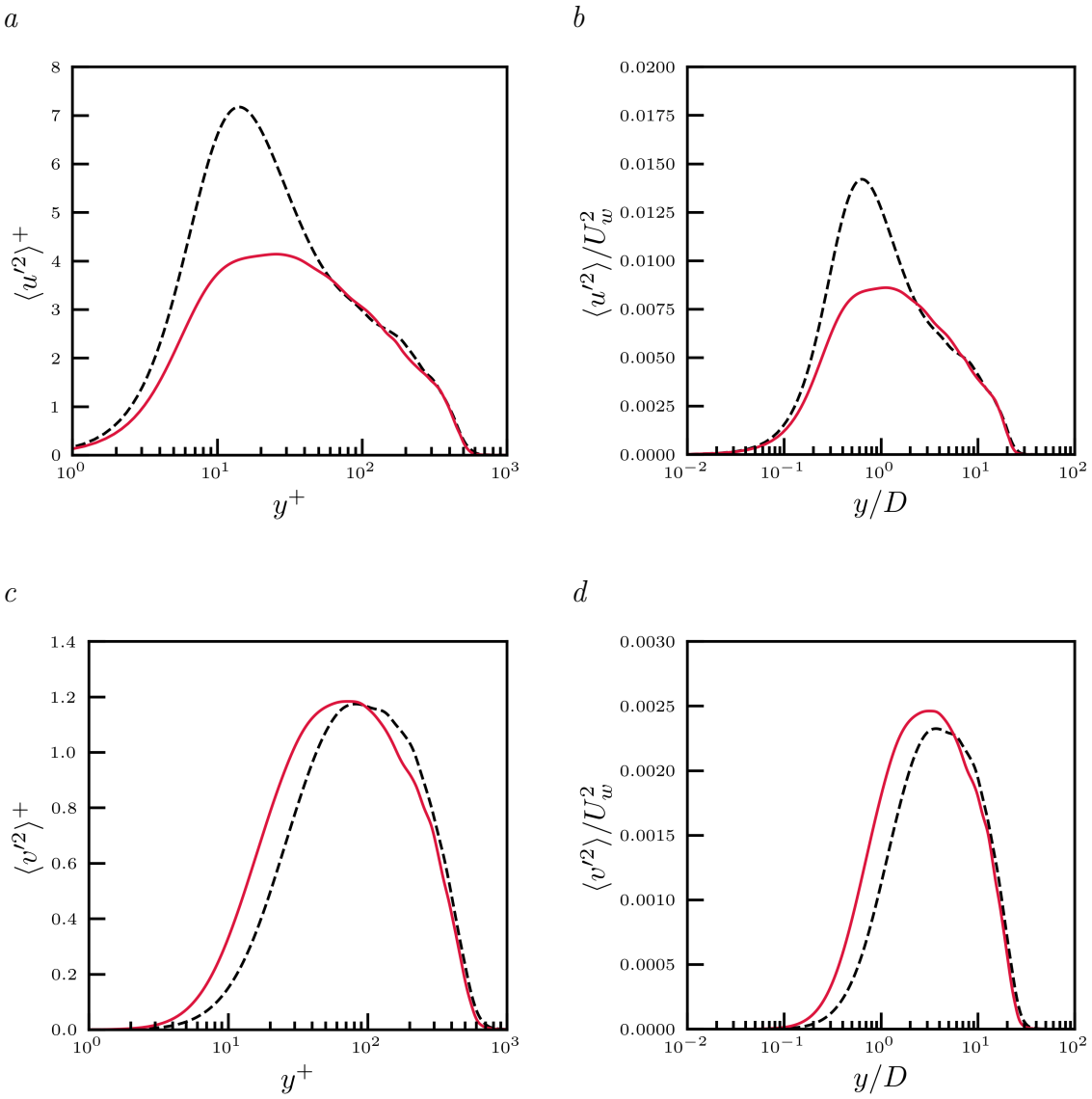


Figure 5.14: FW and TW-DI cases comparison. Black dashed line represents FW at $Re_\tau = 533$; Magenta line represents TW-DI at $Re_\tau = 520$. (a,b) Streamwise velocity variance; (c,d) Wall-normal velocity variance. Left column (a,c) shows inner scaling through actual friction velocity; right column (b,d) shows external scaling.

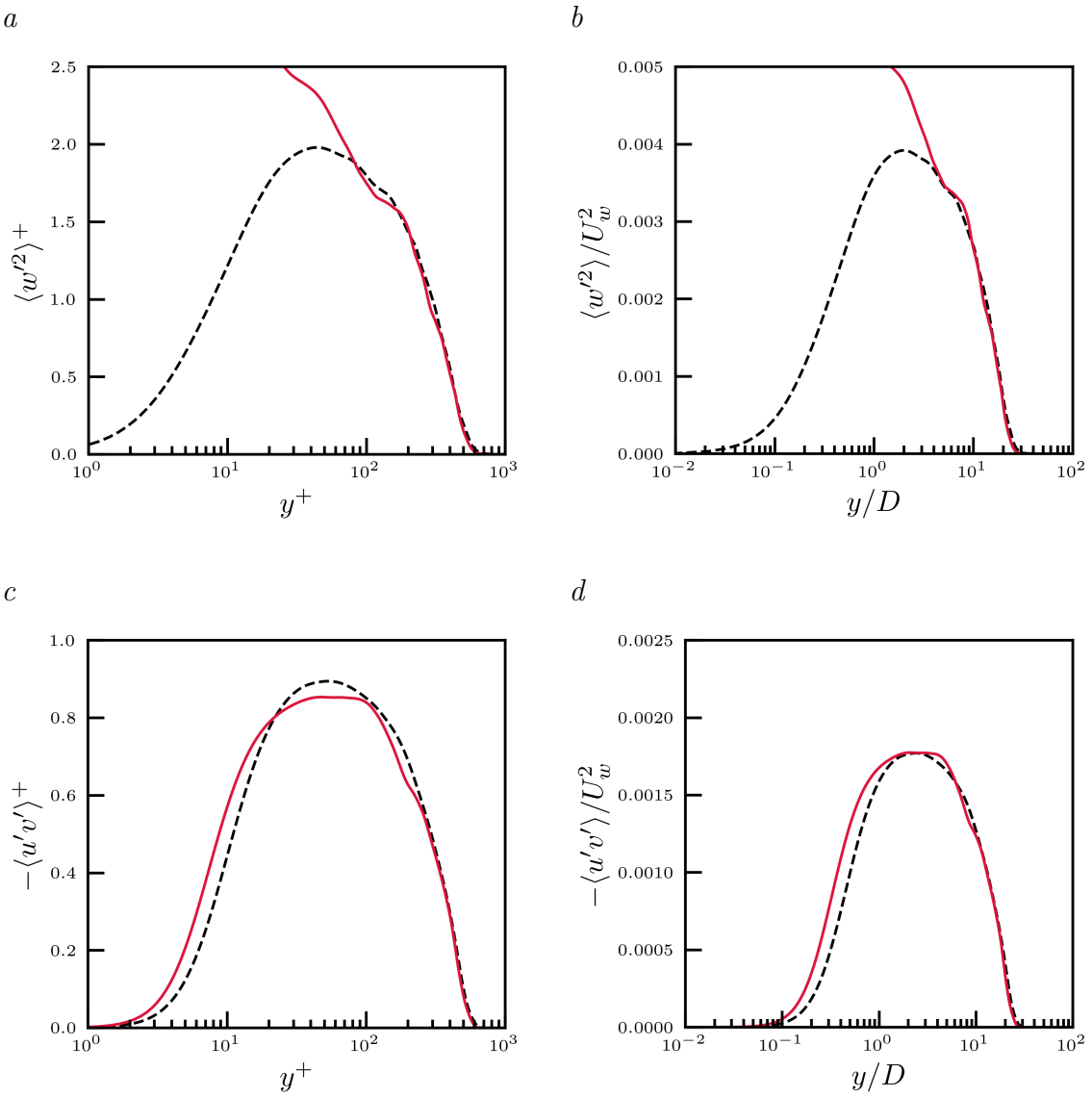


Figure 5.15: FW and TW-DI cases comparison. Black dashed line represents FW at $Re_\tau = 533$; Magenta line represents TW-DI at $Re_\tau = 520$. (a,b) Spanwise velocity variance; (c,d) Reynolds stress. Left column (a,c) shows inner scaling through actual friction velocity; right column (b,d) shows external scaling.

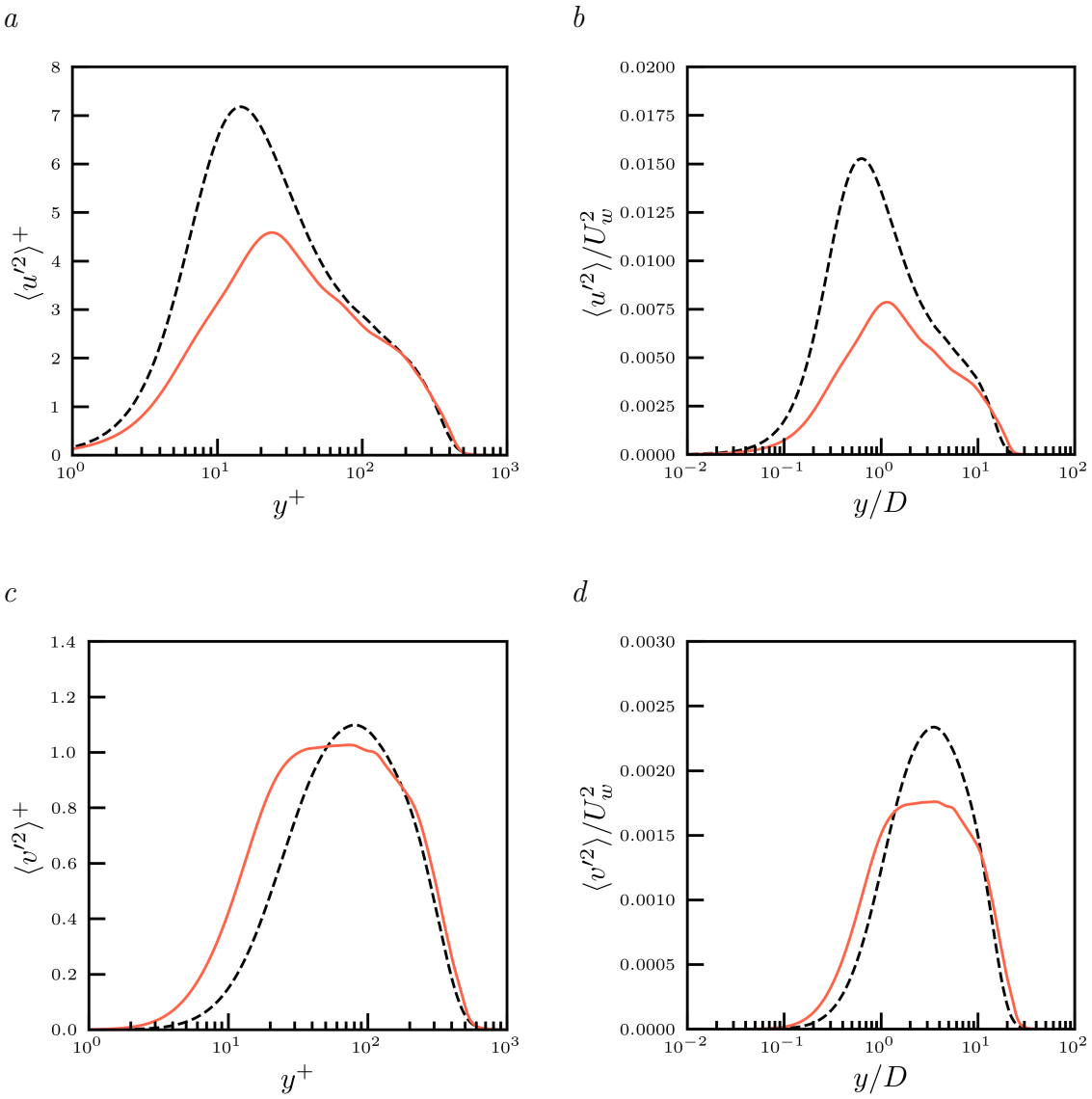


Figure 5.16: FW and TW-DR cases comparison. Black dashed line represents FW at $Re_\tau = 424$; Red line represents TW-DR at $Re_\tau = 455$. (a,b) Streamwise velocity variance; (c,d) Wall-normal velocity variance. Left column (a,c) shows inner scaling through actual friction velocity; right column (b,d) shows external scaling.

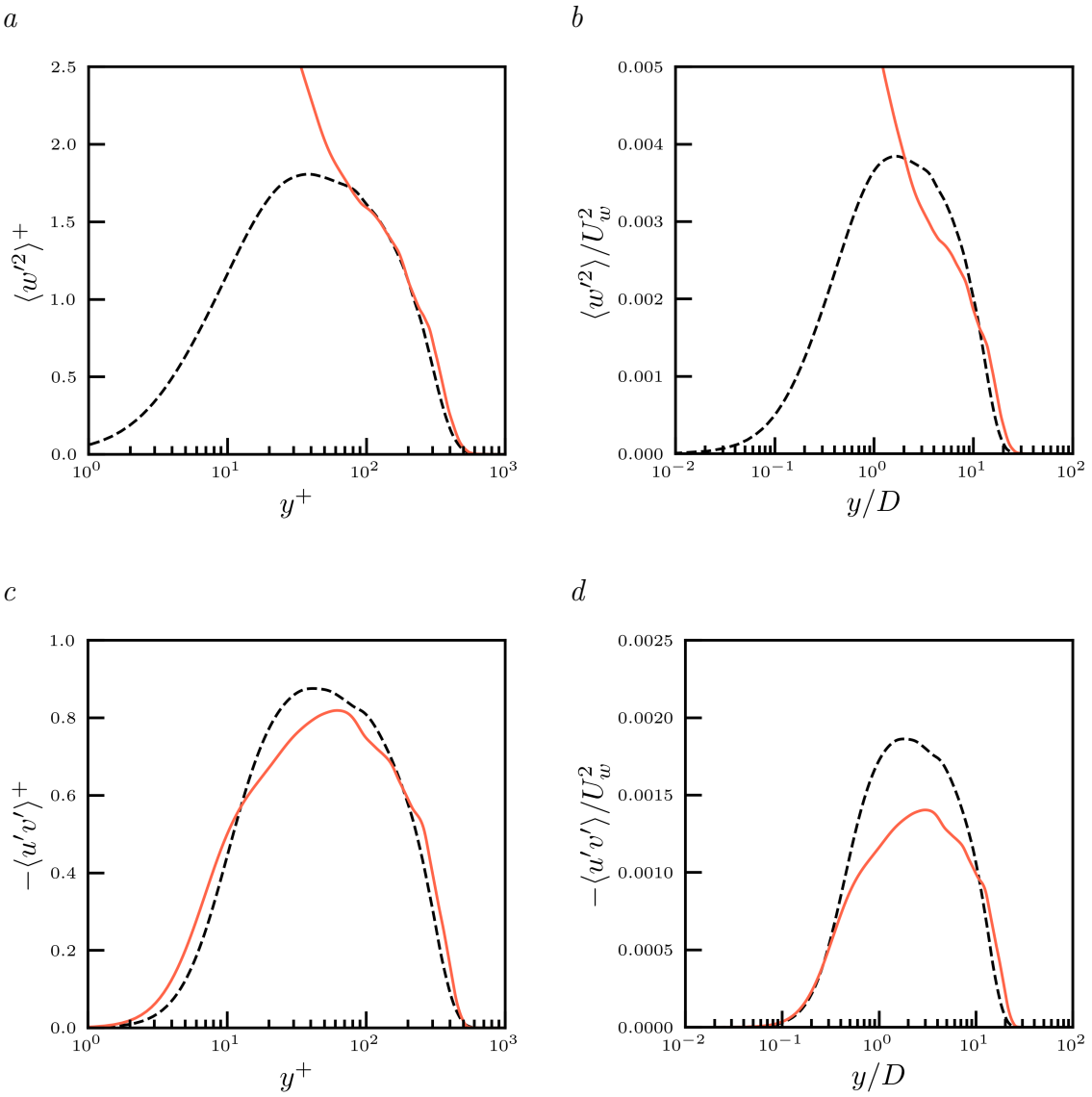


Figure 5.17: FW and TW-DR cases comparison. Black dashed line represents FW at $Re_\tau = 424$; Red line represents TW-DR at $Re_\tau = 455$. (a,b) Spanwise velocity variance; (c,d) Reynolds stress. Left column (a,c) shows inner scaling through actual friction velocity; right column (b,d) shows external scaling.

Chapter 6

Alternative perspective on drag reduction: momentum flux decomposition

Inner scaled statistics of controlled cases, when compared to their respective uncontrolled cases, showed modest variations if compared to greater differences of time evolution quantities, above all skin friction coefficient c_f. To better investigate drag reduction, Moroni et al. (2026) presented an alternative perspective based on the identification of an observable quantity whose variation was the same order of magnitude as that of the skin friction coefficient. With the aim of providing a more comprehensive understanding of the underlying physics, rather than establish an its exact explanation, we build upon the momentum flux decomposition recently introduced by Moroni et al. (2026). Unlike traditional spatial integral decompositions — such as the FIK identity or the Renard and Deck formulation — which collapse the boundary layer dynamics into a single global value integrated up to the boundary layer edge — the proposed approach expresses the skin friction coefficient c_f as a function of the wall-normal coordinate y.
Starting from the mean streamwise momentum equation for TTBLs:

$$\frac{\partial U}{\partial t} = \nu \frac{\partial^2 U}{\partial y^2} - \frac{\partial}{\partial y}\langle u'v' \rangle \tag{6.1}$$

and integrating from the wall ($y = 0$) up to an arbitrary wall-normal distance y, we obtain the exact identity derived by Moroni et al. (2026):

$$c_f = \frac{2}{U_w^2}\left(\nu \frac{\partial U}{\partial y} - \langle u'v' \rangle - \frac{\partial}{\partial t}\int_0^y U(\tilde{y}, t) d\tilde{y}\right) \tag{6.2}$$

This equation demonstrates that at any given distance y from the wall, the total momentum flux matching c_f is split into three distinct physical contributions: diffusive (viscous) momentum flux, $\nu\frac{\partial U}{\partial y}$, which dominates in the near-wall region; turbulent momentum flux: $-\langle u'v'\rangle$, representing the Reynolds shear stress and temporal variation of mean momentum: $-\frac{\partial}{\partial t}\int_0^y U(\tilde{y},t)d\tilde{y}$, accounting for unsteadiness and temporal growth.

This formulation allows to directly observe how the diffusive layer thickens and how momentum flux is handed over to non-viscous mechanisms at the cross-over distance y_{co}. It is defined as the wall distance at which both fluxes, viscous diffusion ($-\nu\partial U/\partial y$) and turbulent shear stress ($-\langle u'v'\rangle$), are equal. Viscous diffusion governs momentum transport within the inner layer ($y < y_{co}$), whereas turbulent mixing dominates farther from the wall ($y > y_{co}$). Under active wall control, the attenuation of near-wall turbulence thickens the viscous-dominated layer, shifting y_{co} farther outward ($y_{co,ow} > y_{co,fw}$). Since the mean velocity profile grows monotonically with wall distance, a larger y_{co} corresponds to a higher mean velocity at the cross-over location (U_{co}). Following the Boussinesq eddy-viscosity concept, the turbulent shear stress scales with the mean velocity jump across the turbulence-dominated region, $\Delta U_{turb} = U_\infty - U_{co}$. As U_{co} increases, the available velocity difference ΔU_{turb} shrinks, directly suppressing the intensity of turbulent momentum transport. To maintain overall momentum balance, this reduction in outer turbulent mixing forces a downward readjustment of the viscous shear stress right at the wall ($\mu\,\partial U/\partial y|_{y=0}$), directly driving the drop in skin friction (cf).

While formulation of Moroni et al. (2026) provides a remarkably clear picture for canonical zero-pressure-gradient (ZPG) cases, this work extends this decomposition by explicitly introducing the mean streamwise pressure gradient $\frac{\partial \bar{p}}{\partial x}$ into the local momentum balance. Considering the mean streamwise momentum equation with an external pressure force:

$$\frac{\partial U}{\partial t} = -\frac{1}{\rho}\frac{\partial P}{\partial x} + \nu\frac{\partial^2 U}{\partial y^2} - \frac{\partial}{\partial y}\langle u'v'\rangle \tag{6.3}$$

Integrating from the wall ($y = 0$) to an arbitrary distance $\bar{y}$ and non-dimensionalizing by the dynamic pressure $\frac{1}{2}\rho U_{ref}^2$, the skin friction decomposition as a direct additive four-component balance is formulated as follows:

$$C_f = \frac{2}{\rho U_{ref}^2}\left[\mu\frac{\partial U}{\partial y}\bigg|_{y=\bar{y}} - \rho\langle u'v'\rangle|_{y=\bar{y}} - \frac{\partial P}{\partial x}\bar{y} - \int_0^{\bar{y}}\rho\frac{\partial U}{\partial t}dy\right] \tag{6.4}$$

This formulation offers two major physical and analytical advantages:

1. Explicit Linear Scaling with y: keeping the pressure term $-\frac{\partial P}{\partial x}\bar{y}$ inside the bracket explicitly shows that the torque exerted by the pressure gradient grows linearly with distance from the wall $\bar{y}$, leaving the outer scaling factor $\frac{2}{\rho U_{ref}^2}$ purely global and constant;

2. Clean additive independence: the skin friction is partitioned into four decoupled contributions:

$$C_f = C_{f,\text{viscous}} + C_{f,\text{turbulent}} + C_{f,\text{pressure}} + C_{f,\text{unsteady}} \tag{6.5}$$

This decomposition is numerically promising and aims to provide a more intuitive understanding of the physical mechanisms governing skin friction in turbulent boundary layers, especially under the influence of adverse pressure gradients and active flow control techniques.
Here follows its application to the present TTBL cases.
First of all the focus is placed on OW and TW simulations, which are eventually compared given the similar friction Reynolds number with the aim of confirming the findings of Moroni et al. (2026).
Figure 6.1 shows the skin friction decomposition for the OW case, which confirms Moroni et al. (2026)'s results. In fact, the viscous sublayer is thickened and the cross-over distance y_{co} is shifted outward. Moreover, it corresponds to a higher mean velocity U_{co}, which reduces the available velocity difference ΔU_{turb} and thus the turbulent momentum flux (see figure 6.1b).

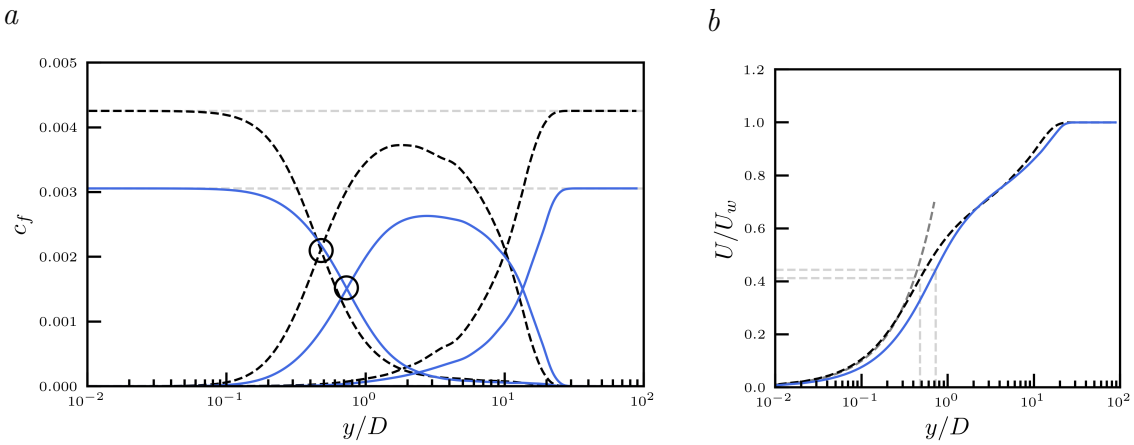


Figure 6.1: (a) Skin friction decomposition. (b) Mean velocity profile in external scaling. Black dashed line represents FW at $Re_\tau = 424$; Blue line represents OW at $Re_\tau = 429$

When the same decomposition is applied to the TW-DR case, however, a different

scenario emerges. As shown in figure 6.2, the cross-over distance y_{co} is not shifted outward, as in the OW case, and the mean velocity at the cross-over location U_{co} is lower than that of the uncontrolled FW case. which increases the available velocity difference ΔU_{turb} and thus the turbulent momentum flux. (see figure 6.2b).

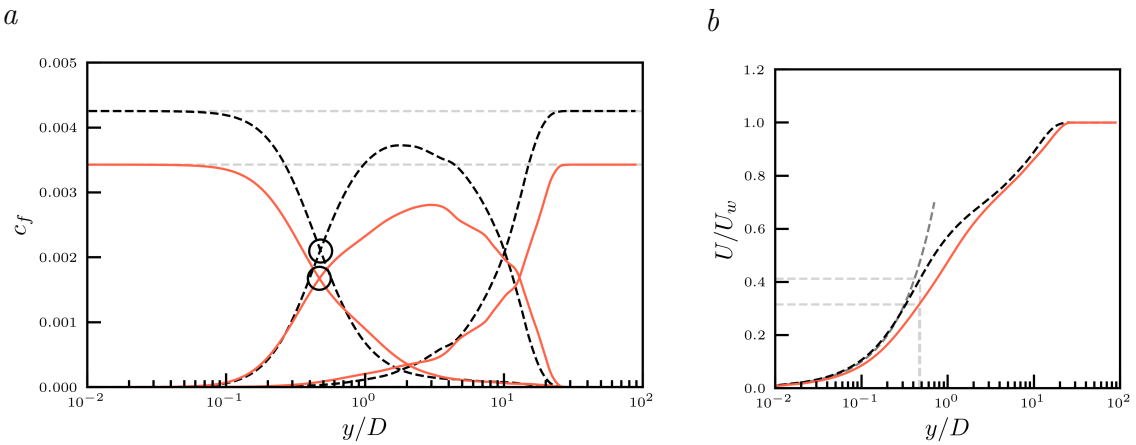


Figure 6.2: (a) Skin friction decomposition. (b) Mean velocity profile in external scaling. Black dashed line represents FW at $Re_\tau = 424$; Red line represents TW-DR at $Re_\tau = 455$

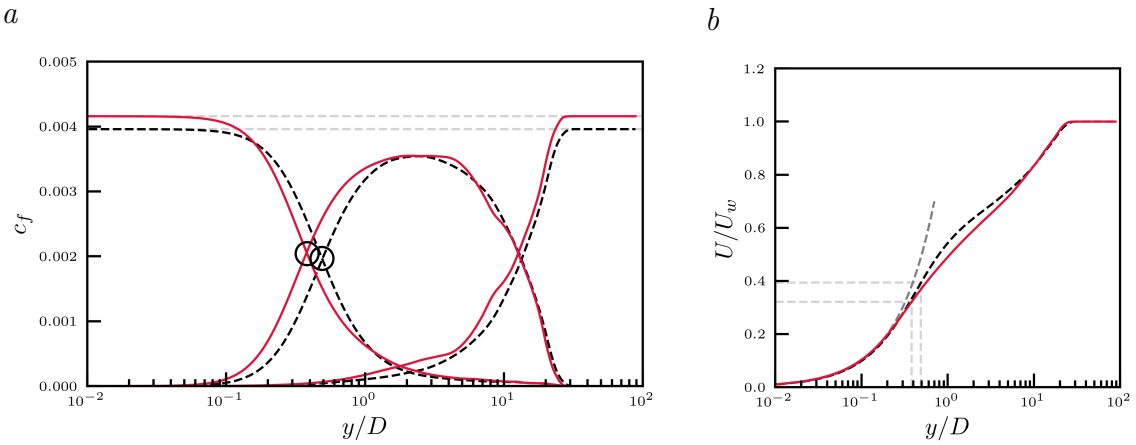


Figure 6.3: (a) Skin friction decomposition. (b) Mean velocity profile in external scaling. Black dashed line represents FW at $Re_\tau = 533$; Magenta line represents TW-DI at $Re_\tau = 520$

Skin friction decomposition applied to the TW-DI case, shows that the cross-over distance y_{co} is shifted inward, corresponding to a lower mean velocity U_{co}, which increases the available velocity difference ΔU_{turb} and thus the turbulent momentum flux (see figure 6.3b).

6.1 Comparative Momentum Analysis

To provide a more comprehensive insight of the physical mechanisms governing wall-bounded flows under adverse pressure gradient, the respective cases, APG and OW-APG are investigated through the lens of the momentum flux decomposition. The analysis is structured around the following observations and interpretations:

1. Cross-over distance Shift (y_{co}): In the pure APG case, the cross-over distance y_{co} undergoes only a minimal outward shift relative to the canonical zero-pressure-gradient baseline. Conversely, when wall oscillations are activated (OW-APG), the generation of a Generalized Stokes Layer induces a substantial outward displacement of y_{co}, physically expanding the viscous-dominated inner region.

2. Cross-over velocity response U_{co}: Examining the mean velocity profiles reveals that the cross-over velocity U_{co} in APG-influenced flows is lower than in the uncontrolled ZPG baseline. In the canonical ZPG framework of Moroni et al. (2026), Boussinesq's eddy-viscosity assumption dictates that Reynolds shear stresses are related to the mean velocity gradient $\partial U/\partial y$ and therefore associated with $\Delta U_{turb} = U_\infty - U_{co}$. Under ZPG assumptions, a lower U_{co} would indicate an increase in ΔU_{turb}, enhancing turbulent momentum exchange and leading to an increase in the skin-friction coefficient (c_f).

3. Pressure gradient contribution: What previously mentioned does not occur because the momentum flux contribution associated with the adverse pressure gradient, scaling linearly with wall distance ($-\frac{\partial P}{\partial x}y$), becomes active directly within the viscous sublayer ($y \to 0$). Acting with a negative sign, this term directly interferes with the local balance between viscous diffusion and turbulent momentum transfer, progressively dominating the momentum budget as y increases.

4. Mean-velocity lift in OW-APG vs. pure APG: When comparing OW-APG directly to pure APG, U_{co} (and the local mean velocity profile) is notably higher in the presence of wall oscillations. This occurs because the Stokes layer "prepares the field"by suppressing near-wall turbulent fluctuations. The higher U_{co} reduces the velocity jump $\Delta U_{turb} = U_\infty - U_{co}$ that turbulence must transport across the boundary layer, which, following the Boussinesq argument above, corresponds to a lower turbulent momentum flux and therefore to a lower skin friction. Moreover, the negative contribution of the pressure gradient acts on a turbulent momentum flux that the oscillation has already reduced,

so the two effects add up and result in a larger reduction of c_f than in either the OW or the APG case alone.

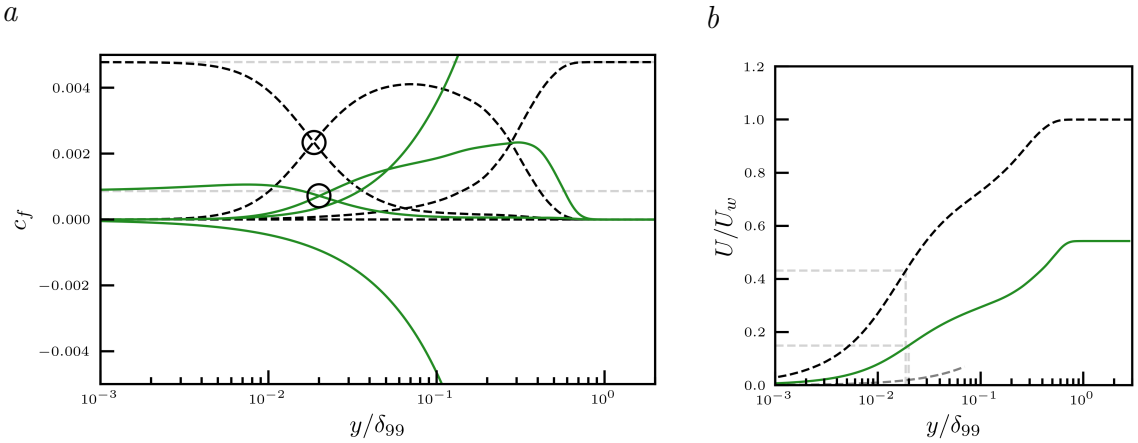


Figure 6.4: (a) Skin friction decomposition. (b) Mean velocity profile in external scaling. Black dashed line represents FW at $Re_\tau = 303$; Green line represents APG at $Re_\tau = 281$

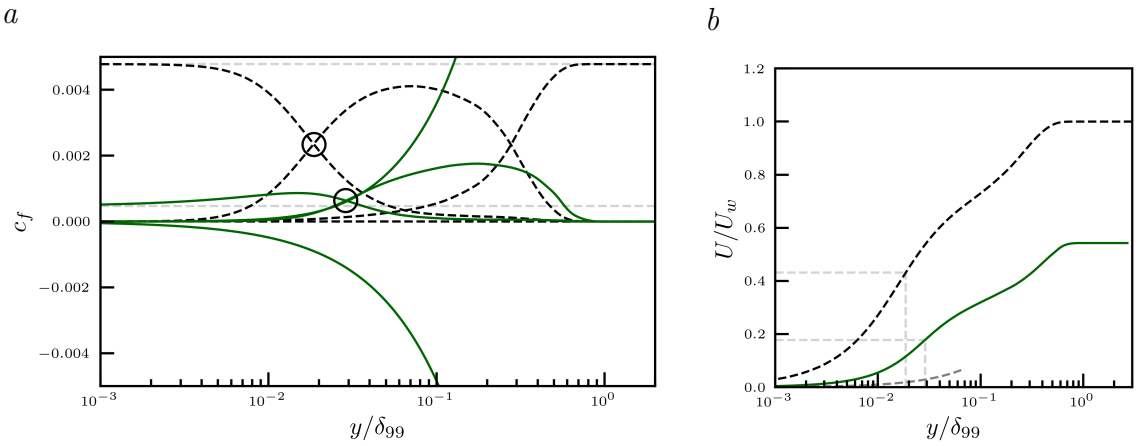


Figure 6.5: (a) Skin friction decomposition. (b) Mean velocity profile in external scaling. Black dashed line represents FW at $Re_\tau = 303$; Darkgreen line represents OW-APG at $Re_\tau = 219$

In summary, this exact momentum flux decomposition confirms and enriches our understanding of boundary layer behavior under adverse pressure gradients, both with and without spanwise wall forcing. In line with the intentions of Moroni et al. (2026), this perspective does not aim to provide a universal explanation for drag reduction, but rather serves as a practical framework to better comprehend turbulent boundary layer dynamics.

Chapter 7

Conclusions and future developments

Channel flows have long served as the benchmark configuration for numerical investigations of wall-bounded turbulence and flow control strategies, primarily due to their spatial homogeneity and reduced computational cost. However, realistic aerodynamic applications involve turbulent boundary layers (TBL), which grow spatially, experience pressure gradients, and are prone to flow separation. The present work addresses this gap by investigating the impact of spanwise wall forcing—specifically, purely temporal wall oscillations (OW) and streamwise-traveling waves of spanwise velocity (STW)—on a turbulent boundary layer subjected to an adverse pressure gradient (APG), utilizing Direct Numerical Simulations (DNS) within a temporally developing boundary layer (TTBL) framework.

Main Findings

Validation of the Temporal Framework. The TTBL approach is confirmed to be a robust, high-fidelity surrogate for spatially developing boundary layers. Once initial condition transients decay ($Re_\theta > 500$), the framework accurately reproduces one-point turbulence statistics, skin-friction evolution, and pressure-gradient dynamics (such as skin-friction collapse and outer-peak emergence) for both uncontrolled and controlled flows. Crucially, this is achieved at a fraction of the computational cost of spatial DNS, validating TTBL as an efficient diagnostic tool for active flow control.
Spanwise Wall Oscillations under APG. Imposing spanwise wall motion under adverse pressure gradients reduces the near-wall skin friction, but does not prevent the near-wall deceleration induced by the pressure gradient. The active forcing anticipates flow separation: the wall shear stress is lowered by the control and the

adverse pressure gradient then drives it to zero sooner.

Streamwise-traveling Waves. For streamwise-traveling waves, control effectiveness exhibits a dependence on both forcing frequency ω and wavenumber k_x. The TTBL framework successfully captures both Drag Reduction (DR) and Drag Increase (DI) regimes, demonstrating excellent agreement with the canonical (ω, k_x) parameter maps established in channel flows (Quadrio et al. 2009) and spatial boundary layers (Skote 2022). Preliminary results for the TW-APG configuration indicate a delay of separation with respect to the only available uncontrolled APG simulation; this rests on a single comparison and is to be regarded as a preliminary indication.

Future Developments

Several promising avenues emerge to extend and refine the findings of this work:

- **Phase-Locked Sampling along $\xi = x - ct$.** Current statistics rely on spatial averaging over x–z planes. A future update to the post-processing code should first map raw fields onto the phase coordinate $\xi = x - ct$ and average over (ξ, y), enabling the isolation of wave-coherent motion from stochastic turbulence and resolving phase-dependent second-order statistics.
- **Systematic (ω, k_x) Parametric Mapping.** Completing a comprehensive drag-reduction map across the (ω, k_x) plane within the TTBL framework will provide a direct comparison with canonical channel maps (Quadrio et al. 2009), clarifying how adverse pressure gradients alter optimal wave parameters and phase speed boundaries.
- **Extended OW-APG Parameter Exploration.** Conducting additional simulations across a broader grid of amplitude and frequency pairs (A^+, T^+) will clarify the functional dependence of anticipation of separation and net power savings on the forcing parameters.
- **Comprehensive TW-APG Investigation.** Expanding the TW-APG analysis—particularly within the optimal drag-reduction regime—will establish whether traveling waves can outperform uniform wall oscillations in suppressing or delaying APG-induced flow separation.
- **Further Assessment of the TTBL Framework under Strong APG.** Additional investigations under stronger or non-equilibrium pressure gradient conditions will further establish the operational boundaries and scaling laws of the temporal boundary layer surrogate model.

Bibliography

Agostini, L. and Leschziner, M. (2018). "The impact of footprints of large-scale outer structures on the near-wall layer in the presence of drag-reducing spanwise wall motion." In: *Flow Turb. Combust.* 100, pp. 1037–1061.

Biau, D. (2023). "Self-similar temporal turbulent boundary layer flow." In: *Comput. Fluids* 254, p. 105795.

Cesari, A. (2026). "High-fidelity simulations for turbulent boundary layers with adverse pressure gradient." MA thesis. University of Modena and Reggio Emilia, UNIMORE.

Choi, K.-S. and Clayton, B. (2001). "The mechanism of turbulent drag reduction with wall oscillation." In: *Int. J. Heat Fluid Flow* 22, pp. 1–9.

Choi, K.-S., DeBishop, J. R., and Clayton, B. (1998). "Mechanisms of drag reduction in turbulent flows with polymer additives." In: *AIAA J.* 36, pp. 1157–1163.

Cimarelli, A., Boga, G., Pavan, A., Costa, P., and Stalio, E. (2024). "Energy cascade phenomena in temporal boundary layers." In: *Flow Turb. Combust.* 112(1), pp. 129–145.

Dhanak, R. and Si, C. (1999). "On reduction of turbulent wall friction through spanwise wall oscillations." In: *Phys. Fluid Mech.* 383, pp. 175–195.

Du, Y. and Karniadakis, G. E. (2000). "Suppressing wall-turbulence via a transverse traveling wave." In: *Science* 288, pp. 1230–1234.

Du, Y., Symeonidis, V., and Karniadakis, G. E. (2002). "Drag reduction in wall-bounded turbulence via a transverse traveling wave." In: *J. Fluid Mech.* 457, pp. 1–34.

Elnahhas, A. and Johnson, P. L. (2022). "On the enhancement of boundary layer skin friction by turbulence: an angular momentum approach." In: *J. Fluid Mech.* 940, A36.

Gómez, T., Flutet, V., and Sagaut, P. (2009). "Contribution of Reynols stress distribution to the skin friction in compressible turbulent channel flows." In: *Phys. Rev. E* 79.

Jiménez, J. and Pinelli, A. (1997). "Wall Turbulence: How it Works and How to Damp it." In: *AIAA Paper 97-2112*.

— (1999). "The autonomous cycle of near-wall turbulence." In: *J. Fluid Mech.* 389, pp. 335–359.

Jung, W., Mangiavacchi, N., and Akhavan, R. (1992). "Suppression of turbulence in wall-bounded flows by high frequency spanwise oscillations." In: *Phys. Fluids A: Fluid Dyn.* 4(8), pp. 1605–1607.

Karniadakis, G. and Choi, K.-S. (2003). "Mechanisms on transverse motion in turbulent wall flows." In: *Annu. Rev. Fluid Mech.* 35, pp. 45–62.

Kim, J. and Hussain, F. (1993). "Propagation velocity and space-time correlation of perturbations in turbulent channel flow." In: *Phys. Fluids A* 5(3), pp. 695–706.

Kitsios, V., Atkinson, C., Sillero, J. A., Borrell, G., Gungor, A. G., Jiménez, J., and Soria, J. (2016). "Direct numerical simulation of a self-similar adverse pressure gradient turbulent boundary layer." In: *Int. J. Heat Fluid Flow* 61 (A), pp. 129–136.

Kitsios, V., Sekimoto, A., Atkinson, C., Sillero, J. A., Borrell, G., Gungor, A. G., Jiménez, J., and Soria, J. (2017). "Direct numerical simulation of a self-similar adverse pressure gradient turbulent boundary layer at the verge of separation." In: *J. Fluid Mech.* 829, pp. 392–419.

Kline, S. J., Reynolds, W. C., Schraub, F. A., and Runstadler, P. W. (1967). "The structure of turbulent boundary layers." In: *J. Fluid Mech.* 30(4), pp. 741–773.

Kozul, M., Chung, D., and Monty, J. (2016). "Direct numerical simulation of the incompressible temporally developing turbulent boundary layer." In: *J. Fluid Mech.* 796, pp. 437–472.

Laadhari, A., Skandaji, L., and Morel, R. (1994). "Turbulence reduction in a boundary layer by a local spanwise oscillating surface." In: *Phys. Fluids* 6(10), pp. 3218–3220.

Laizet, S. and Lamballais, E. (2009). "High-order compact schemes for incompressible flows: A simple and efficient method with quasi-spectral accuracy." In: *J. Comput. Phys.* 228(16), pp. 5989–6015.

Moin, P., Shih, T.-H., Driver, D., and Mansour, N. N. (1990). "Direct numerical simulation of a three-dimensional turbulent boundary layer." In: *Phys. Fluids A: Fluid Dyn.* 2(10), pp. 1846–1853.

Moroni, F., Boga, G., Cimarelli, A., and Stalio, E. (2026). "Drag reduction through wall oscillations in temporal turbulent boundary layers." In: *submitted to J. Fluid Mech.*

Pauley, L. L., Moin, P., and Reynolds, W. C. (1990). "The structure of two-dimensional separation." In: *J. Fluid Mech.* 220, pp. 397–411.

Quadrio, M. and Ricco, P. (2004). "Critical assessment of turbulent drag reduction through spanwise wall oscillations." In: *J. Fluid Mech.* 521, pp. 251–271.

— (2011). "The laminar generalized Stokes layer and turbulent drag reduction." In: *J. Fluid Mech.* 667, pp. 135–157.

Quadrio, M., Ricco, P., and Viotti, C. (2009). "Streamwise-traveling waves of spanwise wall velocity for turbulent drag reduction." In: *J. Fluid Mech.* 627, pp. 161–178.

Quadrio, M., Viotti, C., and Luchini, P. (2007). "Skin-friction drag reduction via steady streamwise oscillations of spanwise velocity." In: *Advances in Turbulence XI ed. J. M. L. Palme and A. Silvia Lopez Springler*, pp. 659–661.

Renard, N. and Deck, S. (2016). "A theoretical decomposition of mean skin friction generation into physical phenomena across the boundary layer." In: *J. Fluid Mech.* 790, pp. 339–367.

Ricco, P. and Quadrio, M. (2008). "Wall-oscillation conditions for drag reduction in turbulent channel flow." In: *Int. J. Heat Fluid Flow* 29, pp. 601–612.

Ricco, P. and Skote, M. (2022). "Integral relations for the skin-friction coefficient of canonical flows." In: *J. Fluid Mech.* 943, A50.

Ricco, P., Skote, M., and Leschziner, M. A. (2021). "A review of turbulent skin-friction drag reduction by near-wall transverse forcing." In: *Prog. Aerosp. Sci.* 123.

Schoppa, W. and Hussain, F. (2002). "Coherent structure generation in near-wall turbulence." In: *J. Fluid Mech.* 453, pp. 57–108.

Skote, M. (2011). "Turbulent boundary layer flow subject to streamwise oscillation of spanwise wall-velocity." In: *Phys. Fluids* 23, p. 081703.

— (2012). "Temporal and spatial transients in turbulent boundary layer flow over an oscillating wall." In: *Int. J. Heat Fluid Flow* 38, pp. 1–12.

— (2013). "Comparison between spatial and temporal wall oscillations in turbulent boundary layer flows." In: *J. Fluid Mech.* 730, pp. 273–294.

— (2022). "Drag reduction of turbulent boundary layers by traveling and non-traveling waves of spanwise wall oscillations." In: *Fluids.* 7(65).

Skote, M. and Henningson, D. S. (2002). "Direct numerical simulation of a separated turbulent boundary layer." In: *J. Fluid Mech.* 471, pp. 107–136.

Skote, M., Mishra, M., and Wu, Y. (2015). "Drag reduction of a turbulent boundary layer over an oscillating wall and its variation with reynolds number." In: *Int. J. Aerosp. Eng.*

Skote, M., Mishra, M., and Wu, Y. (2019). "Wall oscillation induced drag reduction zone in a turbulent boundary layer." In: *Flow Turbul. Combust.* 102(3), pp. 641–666.

Smith, C. R. and Metzler, S. P. (1983). "The characteristics of low-speed streaks in the near-wall region of a turbulent boundary layer." In: *J. Fluid Mech.* 129, pp. 27–54.

Spalart, P. R. (1988). "Direct numerical simulation of a turbulent boundary layer up to $Re_\theta = 1410$." In: *J. Fluid Mech.* 187, pp. 61–98.

Spalart, P. R. and Strelets, M. K. (2000). "Mechanisms of transition and heat transfer in a separation bubble." In: *J. Fluid Mech.* 403, pp. 329–349.

Touber, E. and Leschziner, M. A. (2012). "Near-wall streak modification by spanwise oscillatory wall motion and drag-reduction mechanisms." In: *J. Fluid Mech.* 693, pp. 150–200.

Viotti, C., Quadrio, M., and Luchini, P. (2008). "Streamwise oscillation of spanwise velocity at the wall of a channel for turbulent drag reduction." In: *Phys. Fluids* 20.

Wu, W., Meneveau, C., and Mittal, R. (2020). "Spatio-temporal dynamics of turbulent separation bubbles." In: *J. Fluid Mech.* 883, A45.

Yang, Q. and Hwang, Y. (2019). "Modulation of attached exact coherent states under spanwise wall oscillation." In: *11th Int. Symp.*

Yudhistitra, I. and Skote, M. (2011). "Direct numerical simulation of a turbulent boundary layer over an oscillating wall." In: *J. Turbul.* 12.

Zhang, J., Xiao, D., and Yao, J. (2025). "Reynolds number effect on drag reduction via spanwise wall oscillation in turbulent boundary layers." In: *Phys. Fluids.* 37(4).

Zhang, X., Watanabe, T., and Nagata, K. (2018). "Turbulent/non-turbulent interfaces in high-resolution direct numerical simulation of temporally evolving compressible turbulent boundary layers." In: *Phys. Rev. Fluids.* 3, p. 094605.

— (2023). "Reynolds number dependence of the turbulent/non-turbulent interface in temporally developing turbulent boundary layers." In: *J. Fluid Mech.* 964, A8.